



Article

Inferring 2D Local Surface-Deformation Velocities Based on PSI Analysis of Sentinel-1 Data: A Case Study of Öraefajökull, Iceland

Jirathana Dittrich ^{1,2} , Daniel Hölbling ^{1,*} , Dirk Tiede ¹ and Þorsteinn Sæmundsson ³

¹ Department of Geoinformatics—Z_GIS, University of Salzburg, Schillerstr. 30, 5020 Salzburg, Austria; jirathana.dittrich@alumni.tum.de (J.D.); dirk.tiede@plus.ac.at (D.T.)

² Leibniz Supercomputing Centre (LRZ) of the Bavarian Academy of Sciences and Humanities, Boltzmannstraße 1, 85748 Garching, Germany

³ Department of Geography and Tourism, University of Iceland, Sturlugata 7, 101 Reykjavik, Iceland; steinis@hi.is

* Correspondence: daniel.hoelbling@plus.ac.at

Abstract: Two-dimensional deformation estimates derived from Persistent Scatterer Interferometric (PSI) analysis of Synthetic Aperture Radar (SAR) data can improve the characterisation of spatially and temporally varying deformation processes of Earth's surface. In this study, we examine the applicability of Persistent Scatterer (PS) Line-Of-Sight (LOS) estimates in providing two-dimensional deformation information, focusing on the retrieval of the local surface-movement processes. Two Sentinel-1 image stacks, ascending and descending, acquired from 2015 to 2018, were analysed based on a single master interferometric approach. First, Interferometric SAR (InSAR) deformation signals were corrected for divergent plate spreading and the Glacial Isostatic Adjustment (GIA) signals. To constrain errors due to rasterisation and interpolation of the pointwise deformation estimates, we applied a vector-based decomposition approach to solve the system of linear equations, resulting in 2D vertical and horizontal surface-deformation velocities at the PSs. We propose, herein, a two-step decomposition procedure that incorporates the Projected Local Incidence Angle (PLIA) to solve for the potential slope-deformation velocity. Our derived 2D velocities reveal spatially detailed movement patterns of the active Svínafellsjökull slope, which agree well with the independent GPS time-series measurements available for this area.

Keywords: Persistent Scatterer Interferometry (PSI); Sentinel-1; local deformation; 2D velocity; slope deformation; ellipsoid incidence angle; projected local incidence angle; Iceland



Citation: Dittrich, J.; Hölbling, D.; Tiede, D.; Sæmundsson, Þ. Inferring 2D Local Surface-Deformation Velocities Based on PSI Analysis of Sentinel-1 Data: A Case Study of Öraefajökull, Iceland. *Remote Sens.* **2022**, *14*, 3166. <https://doi.org/10.3390/rs14133166>

Academic Editor: Oriol Monserrat

Received: 6 April 2022

Accepted: 19 June 2022

Published: 1 July 2022

Publisher's Note: MDPI stays neutral with regard to jurisdictional claims in published maps and institutional affiliations.



Copyright: © 2022 by the authors. Licensee MDPI, Basel, Switzerland. This article is an open access article distributed under the terms and conditions of the Creative Commons Attribution (CC BY) license (<https://creativecommons.org/licenses/by/4.0/>).

1. Introduction

Satellite-based Interferometric Synthetic Aperture Radar (InSAR) has been proven to be a valuable tool for detecting subtle deformation of the ground surface at a high spatial resolution, covering large areas, under favourable conditions, with up to sub-centimetre precision [1–4]. A more advanced technique, Multi-temporal InSAR (MTI), has further improved InSAR's applicability in detecting deformation and estimating displacement rates associated with earthquakes or volcanic activity [5–7]; slope instabilities and slow landslide displacements [8–11]; anthropogenically induced subsidence [12–14]; and monitoring critical infrastructures such as buildings and dams [15–17]. Despite promising results in some cases, accurate mapping and monitoring of deformation processes in mountainous environments by means of MTI is still challenging. Constraints are mainly encountered because of Synthetic Aperture Radar (SAR) geometric distortions, e.g., layover and shadow, which reduce SAR-to-target visibility and, therefore, the density of usable Persistent Scatterer (PS). In addition, signal decorrelation occurs due to changes in vegetation cover or fast surface-movements [3,18].

The launches of the Copernicus Sentinel-1 (S-1) radar satellites in 2014 (Sentinel-1A) and 2016 (Sentinel-1B) [19,20] and the provision of a ready-to-use software toolbox, i.e., the SentiNel Application Platform (SNAP) [21,22], have provided the user community with unprecedented SAR data quality and tools allowing deformation studies at low cost. Technically, Sentinel-1 marks a new era, wherein deformation phenomena can be actively observed on a spatially detailed grid (~10 m), with high temporal frequencies (every 6 days) and in two dimensions (2D), wherever both ascending and descending acquisitions are available. Despite the availability of S-1 data in most areas, the applicability and interpretation of MTI-based Line-Of-Sight (LOS) deformation estimates, particularly the 2D characterisation of deformation evolution processes in high relief areas, still need to be researched [23]. Several case studies have applied MTI for hot-spot mapping, landslide characterisation, slope failure prediction, and landslide inventory updating [10,14,23–29]. While research on the continuous, semi-automatic monitoring of slow-moving landslides has been emerging, studies that examine the applicability of 2D decomposition algorithms in areas governed by complex deformation processes are still underrepresented.

Persistent Scatterer Interferometry (PSI) is known as a subcategory of MTI processing. The PSI technique [2,5,30,31] applied in this study relies on the single-master approach, meaning all radar images are co-registered with reference to their master image to form a time-series of interferograms. Only resolution elements (i.e., PS) exhibiting phase stability and a high signal-to-noise ratio (SNR) over the study period are selected and integrated into the PSI analysis. The derivation of LOS deformation estimates is, therefore, possible only on sparse grids of PSs. The Stanford Method for Persistent Scatterers (StaMPS) was selected for this study because it does not require any a priori assumption of the temporal model of deformation. It allows for the extraction of deformation signals that are not necessarily linear with time, e.g., slope deformation related to slow-moving landslides [5,32].

Several studies were carried out to quantify deformation fields in Iceland, with or without applying PSI. Based on countrywide GNSS measurement campaigns (1993, 2004), crustal deformation fields characterising Glacial Isostatic Adjustment (GIA) and plate-spreading velocities were modelled [33]. This work indicated that GIA and plate-spreading movements are major contributors to crustal deformation processes and should not be ignored when interpreting local deformation in Iceland. PSI analysis was previously applied to ERS and Envisat data to derive LOS deformation rates. The study concluded the detected regional uplift trend to be deformation primarily induced by GIA [34]. Recently, PSI analyses of S-1 data (2015–2018) were carried out to derive 2D velocity fields and used to update existing GIA and plate tectonic velocity models [35]. The results indicated the existence of local deformation residuals, interpreted as deformation induced by subsurface rheology variations.

Theoretically, the retrieval of 3D motion vectors (i.e., east, north, and vertical components) from three independent InSAR LOS measurements is possible, provided that multi-geometry data with a satellite inclination of about $60^\circ/120^\circ$ covering the same area are available. The N-S component is known to be the most difficult to determine using data from near-polar orbiting satellites [36,37]. The decomposition of LOS measurements from Sentinel-1 ascending and descending data into a 2D motion vector is crucial for the accurate quantification of 2D deformation fields in this study, mainly for two reasons. First, disregarding the quantification of the horizontal movement, when it is present, would lead to the misinterpretation of the vertical movement. The interpretation error depends on the magnitude of the horizontal movement and steepness of the incidence angle. Second, due to its system configurations, the S-1 LOS measurement is more sensitive to horizontal motion and less sensitive to vertical motion when compared to ERS and TerraSAR-X missions (also known as decomposition sensitivity, cf. Appendix A, Table A1 for further detail).

This research aims to investigate the applicability of the full-resolution, two-dimensional LOS deformation estimates, derived from a state-of-the-art workflow that combines PSI analysis of S-1 data with a vector-based decomposition approach to infer local deformation information, focusing on inclined terrain. We propose a new two-step decomposition

procedure that allows for the isolation of the deformation signal of interest; it incorporates the Project Local Incidence Angle (PLIA) instead of the classical Ellipsoid Incidence Angle (EIA), to directly retrieve the slope-deformation velocity. We test and demonstrate the usability of the proposed algorithm to infer 2D movements in the geomorphologically dynamic Öraefajökull area in Iceland.

In the subsequent sections, the terms “deformation” and “surface movement” (mm) are used interchangeably to describe the estimated surface deformation (mm) from a time-series of interferograms. The terms “deformation rate”, “surface-deformation velocity”, and “motion rate” can be interchangeably used to define the mean velocity (mm/y) as derived over the entire period of an InSAR stack.

2. Materials and Methods

2.1. Study Area

Iceland is traversed by the Mid-Atlantic-Ridge, which forms the plate boundary zone between the North American and Eurasian tectonic plates. Our study area is located west of the Öraefajökull stratovolcano, in the southern part of the Vatnajökull National Park in southeastern Iceland (Figure 1). The Öraefajökull massif is composed of basaltic and silicic rocks (lava flows, hyaloclastite, and intrusions) as well as sedimentary rocks [38]. This area is influenced by the rapid retreat of the Vatnajökull (Vat) glacier, the largest and most voluminous Icelandic glacier, which causes significant isostatic uplift. This uplift—coupled with the steep relief, the large amount of unconsolidated debris, glacial erosion, the thawing of permafrost, and high precipitation—make the Öraefajökull area highly susceptible to slope instability, resulting in landslides and debris flows (e.g., [39,40]). Geodetically, GPS measurement campaigns have been carried out and time-series data from continuous GPS (cGPS) stations across Iceland have been used to quantify the surface deformation due to Glacial Isostatic Adjustment (GIA) and plate-spreading processes at the regional scale [33,41]. Such regional deformation signals characterised by slow, steady movements can usually be well constrained by PSI. Surface deformation induced by seismic events, earthquakes, and volcanic deflation or inflation, depending on its magnitude and duration, also affect the overall deformation field in this area.

2.2. Data

Sentinel-1 radar imagery from the European Copernicus programme (Single-Look Complex (SLC) product, Interferometric Wide (IW) mode) spanning the period from spring 2015 to autumn 2018, for both ascending (A118) and descending (D111) passes, were acquired for the PSI. Only radar data acquired from May to October were considered, to avoid snow-covered areas as much as possible. High- to medium-resolution digital elevation models (DEMs), i.e., the ArcticDEM [42] and TanDEM-X DEM [43] and their derived products, were used for interferometric processing, data analysis and visualisation. Three-dimensional (3D) time-series deformation information at several GPS stations, kindly made available by the Icelandic Meteorological Office (IMO), was used for calibration and validation purposes. Table 1 summarises the data and ancillary data used in this study.

2.3. Methods

The overall processing, validation and analysis workflow consists of five main components: (1) Terrain Observation with Progressive Scans SAR (TOPSAR) pre-processing and InSAR processing [21,44]; (2) PSI analysis with StaMPS; (3) calibration and validation of LOS estimates; (4) vector-based LOS velocity decomposition, including spatial-proximity analysis and a two-step decomposition procedure of LOS deformation vectors into 2D vertical and horizontal deformation velocities; and (5) spatial statistics and spatial analysis to infer the 2D local deformation velocities (cf. Figure 2).

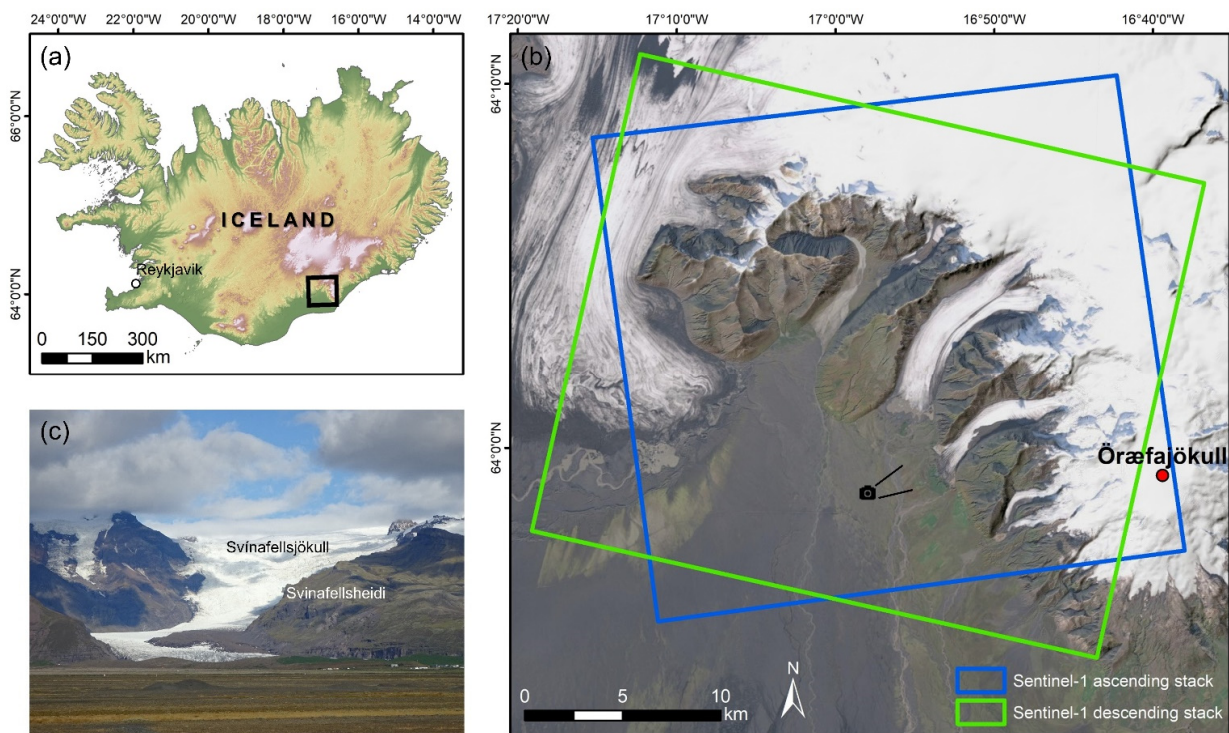


Figure 1. Study area: (a) area of interest (AoI) located in southern Iceland, west of the Öraefajökull volcano which constitutes the southern part of Vatnajökull National Park. The map shows the IS 50 V digital elevation model (DEM) of Iceland underlain by a hillshade (© National Land Survey of Iceland); (b) terrain topography in the AoI consists of outlet glaciers interchanged with mountainous slopes and flat terrain and the footprints of ascending (blue) and descending (green) PSI data stacks. The location from which the photograph in (c) was taken is indicated; (c) field photograph (© D. Hölbling) shows the mountain slope (Svínafellsheiði—SvH) under analysis.

Table 1. Data and ancillary data used for the analysis.

Data	Resolution (m)	Description
Sentinel-1 SAR	2.3×14.1 ¹	Orbit: Ascending (A118) Acquisition time: 29/05/2015–10/09/2018 No. of ifgs ³ : 28 Incidence angle (EIA): 41.2°–45.6° Heading: 350.6°
Sentinel-1 SAR	2.3×14.1 ²	Orbit: Descending (D111) Acquisition time: 17/05/2015–04/10/2018 No. of ifgs: 25 Incidence angle (EIA): 36.0°–41.5° Heading: 191.0°
Arctic-DEM	2	Derived from stereo–optical imagery acquired during 2012–2017
Tandem-X DEM	20	Derived from radar imagery acquired during 2011–2015
GPS deformation time-series ⁴ SKFC ⁵ SVIN SVIE		Observation period: July 2015–October 2018 July 2018–October 2018 July 2018–October 2018

^{1,2} Pixel spacing $r_g \times az$ m; ³ interferograms; ⁴ kindly made available by the Icelandic Meteorological Office (IMO); ⁵ GPS station name.

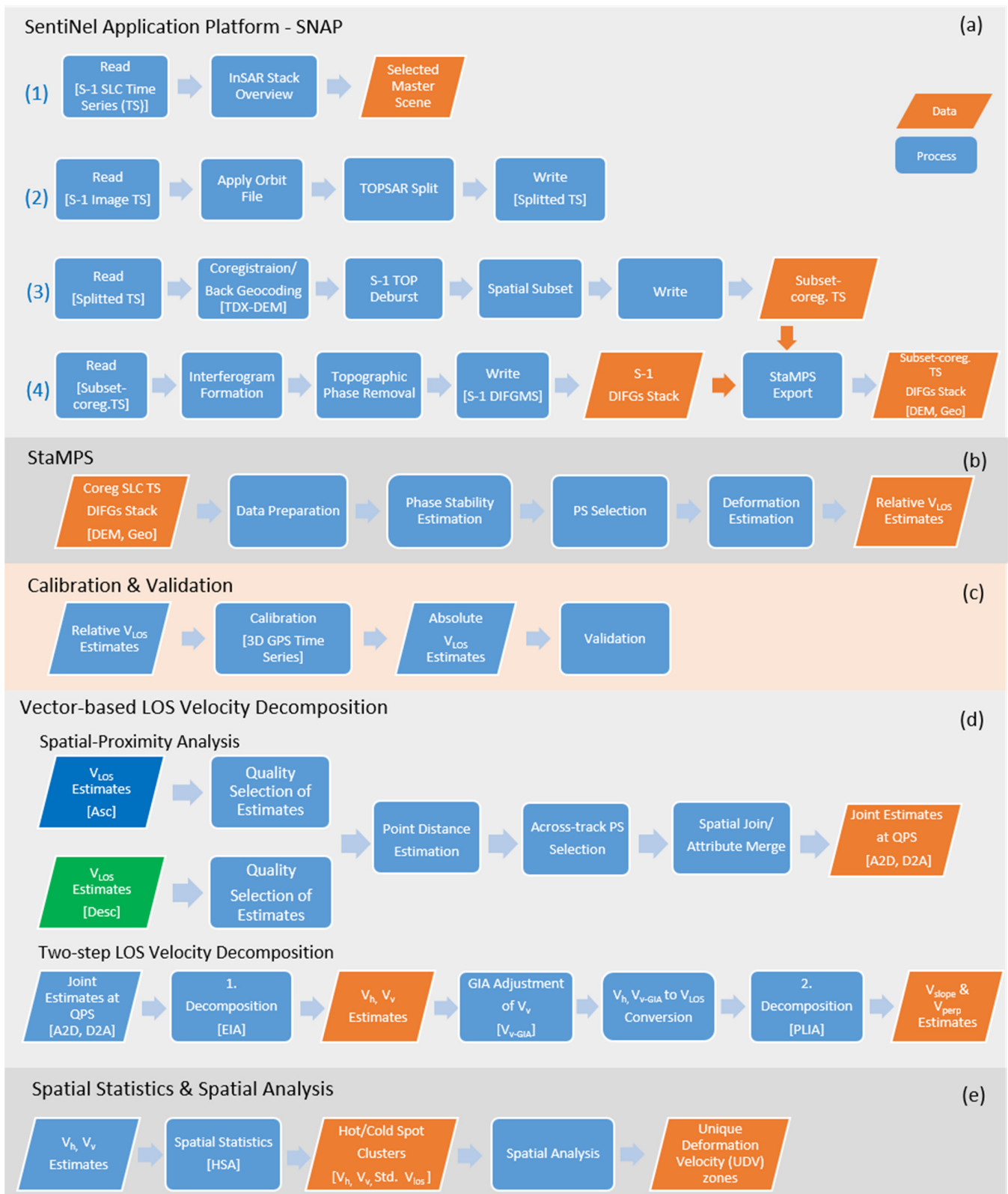


Figure 2. Schematic diagram of data processing, validation and analyses in this study: (a) TOPSAR pre-processing and InSAR processing in SNAP; (b) PSI analysis with StaMPS; (c) calibration and validation; (d) vector-based LOS velocity decomposition; and (e) spatial statistics and spatial analysis.

For simplicity, we divided dedicated pre-processing procedures for TOPSAR data and the generic interferometric processing within SNAP [22,45] into four processing steps. The InSAR stack overview was used to determine the optimal master scenes that minimise the overall signal decorrelation for each S-1 image time-series (ts in Figure 2a). In general, the scene that lay in the middle of the study period was selected. Apply orbit file and TOPSAR Split involve satellite orbit correction and the splitting up of SAR images into smaller parts (subswath and burst) according to the area of interest (AoI). Then S-1 split time-series were coregistered (back geocoding) based on their selected master scene and *spatial subset*. This step requires elevation information of the scene to preserve geolocational accuracy. In our case, the Tandem-X DEM was used. Next, interferogram formation and topographic phase removal were required to generate differential interferograms (DIFGs). Finally, during the StaMPS export, we prepared interferogram stacks (DIFGs stack and co-registered S-1 time series) and associated parameters in compatible formats for further PSI analysis in StaMPS.

PSI was performed using the StaMPS [46] open-source software packages. The main outcome of this analysis is known as the relative deformation rate or mean velocity estimate in the LOS direction. The conceptual basis of the PSI analysis using StaMPS is briefly described in Section 2.3.1. The detailed implementation steps are beyond the scope of this paper and can be found in the StaMPS manual [47]. Calibration and validation of the PS-based estimation results are described in Section “Calibration and Validation of LOS Estimates”.

To constrain propagating errors due to rasterisation and interpolation of the pointwise LOS estimates, the vector-based approach of spatial-proximity analysis described in [48] was implemented. The goals of the analysis were to ensure that LOS estimates of quality PSs (hereafter, QPSs) were exploited, and suitable neighbouring PSs in across-track data were identified. Once neighbouring PSs were identified, the attributes of the centred PS (for example, ascending) and its across-track surrounding PSs (descending) were spatially joined and made available for 2D decomposition. Thus, we can derive 2D deformation velocities at all QPSs available from both ascending (A) and descending (D) data. The proposed algorithm increases the spatial density of measurement points as well as preserving the reliability of the pointwise 2D velocity estimates compared to the rasterised 2D estimates [48]. A schematic representation of the overall processing and analysis workflows is shown in Figure 2.

2.3.1. PSI Analysis for Deriving LOS Deformation Estimates

The wrapped phase ($\psi_{x,i}$) at pixel x in the topographically corrected i th interferogram (the DIFG) is affected by multiple phase contributions and can be written as the wrapped sum of five phase terms [5]

$$\psi_{x,i} = W\{\phi_{D,x,i} + \phi_{A,x,i} + \Delta\phi_{O,x,i} + \Delta\phi_{\theta,x,i} + \phi_{N,x,i}\} \quad (1)$$

where $\phi_{D,x,i}$ is the phase change due to surface movement in the LOS; $\phi_{A,x,i}$ is the phase due to the difference in atmospheric phase delay during the two acquisitions; $\Delta\phi_{O,x,i}$ is the phase due to orbit inaccuracies; $\Delta\phi_{\theta,x,i}$ is the residual phase due to look-angle (DEM) error; $\phi_{N,x,i}$ is the phase noise due to scattering variability, thermal noise, processing errors, etc.; and $W\{\cdot\}$ is the wrapping operator. The first three terms in Equation (1) are spatially correlated. The fourth term is partially spatially correlated. Since we are interested in the first term ($\phi_{D,x,i}$), the deformation, the other terms must be estimated and subtracted from the wrapped phase.

In practice, the following four PS processing tasks are transformed into eight operational steps (steps 1 to 8) within the StaMPS environment, which can be automatically implemented at once, or step-by-step (cf. Figure 2b) [47]. These include:

- Data Preparation, which involves selection of the initial PS Candidates (PSC) and processed-area subsetting (patches).

- Phase Stability Estimation, which includes phase noise estimation for each PSC in every interferogram. Gamma (γ_x), a coherence-like measure, is used to express the phase noise level of a PSC and its possibility to become a PS.
- PS Selection, which determines whether a PSC will be a PS based on their phase noise estimates. Only PSCs with persistent phase stability for the entire period were selected.
- Displacement/Deformation Estimation, which involves deformation signal isolation at PS pixel. This is achieved by unwrapping phase values and by subtracting various unwanted terms.

We applied the suggested (default) processing parameters to derive LOS deformation-rate estimates (aka Mean LOS Velocity (MLV) in StaMPS) of the PSs. We estimated deformation rates with respect to the selected reference point (SKFC), whose available GPS deformation time-series measurements coincided with the InSAR analysis period, i.e., May 2015 to October 2018, for MLV estimation (cf. Table 1).

Calibration and Validation of LOS Estimates

In principle, a SAR sensor can measure only the path length difference in one dimension, i.e., in its LOS (slant range) direction. That is, a three-dimensional (3D) deformation vector (d) with its components in East (d_E), North (d_N), and Up (d_U) is projected in the LOS direction (d_{los}). The LOS deformation vector (d_{los}) can be expressed in relation to its 3D components as [49]:

$$d_{los} = \begin{bmatrix} -\sin \theta \cos \alpha & \sin \theta \sin \alpha & \cos \theta \end{bmatrix} \begin{bmatrix} d_E \\ d_N \\ d_U \end{bmatrix} \quad (2)$$

where θ is the incidence angle and α denotes the satellite's orbit heading (azimuth) measured positive clockwise from the north. Since we are interested in the surface-movement velocity (v), we replace d_{los} in Equation (2) with v_{los} ; the same expression is valid [3,50] and can be written as Equation (3).

$$v_{los} = \begin{bmatrix} -\sin \theta \cos \alpha & \sin \theta \sin \alpha & \cos \theta \end{bmatrix} \begin{bmatrix} v_E \\ v_N \\ v_U \end{bmatrix} \quad (3)$$

Relative LOS estimates as a result of PSI in StaMPS require calibration before further analysis. Based on 3D displacement time-series measurements (d_E , d_N , d_U) and linear regression analysis, the mean velocities (v_E , v_N , v_U) of the SKFC reference point were derived using Equations (2) and (3). Using S-1 parameters, we derived the LOS velocities of SKFC for the ascending and descending InSAR stacks. We then used the obtained LOS estimates (v_{los}) of SKFC to calibrate other relative PS LOS measurements globally, leading to absolute LOS measurements at all PSs.

Validation of the PS MLV estimates was carried out based on the available GPS displacement time-series observations from three reference stations, corresponding to the InSAR time span (cf. Table 1). Using SAR parameters, i.e., incidence angle, azimuth heading, and linear regression analysis, 3D GPS velocities were projected into the LOS direction and used for validation (cf. Equations (2) and (3)). MLV estimates of PSs located within a maximum distance of 250 m with a slope aspect similar to the reference GPS stations were selected for validation purposes.

2.3.2. Decomposition of LOS Deformation Rate Estimates

The vector-based velocity decomposition started with quality PS estimate selection, followed by a spatial-proximity analysis. The proposed two-step vector decomposition was then executed to accommodate GIA-like signal removal and, finally, to obtain the potential "slope-deformation velocity".

Spatial-Proximity Analysis

Two criteria were used to filter good quality PS (QPS) estimates. The standard deviation of v_{los} implies the degree of linearity of the movement, and the layover-shadow mask implies that the PS pixels are affected by geometric distortions. Since the remaining number of PSs on the mountainous slopes should be sufficient and the nonlinear movement of PS is of interest, standard deviation thresholding (percentile 95) and layover-shadow-mask buffering of 100 m were applied to select quality estimates.

The derivation of location-based V_v and V_h at PS started with spatial-proximity analysis. Different spatial search radii between 100 and 300 m (with 50 m steps) were tested to find the optimal distance that balances the number of detectable across-track PSs and the computational time for 2D decomposition at PSs. We executed the searches twice, from ascending to descending (A2D) and descending to ascending (D2A) PSs, to make 2D decomposition possible at all PSs. Once across-track PSs were identified, all their attributes were spatially merged and the pointwise computation of 2D velocity parameters was performed (cf. Equations (4)–(6)).

Two-Step LOS Velocity Decomposition

A SAR sensor can measure only the path length difference in one dimension in the LOS direction. If three independent InSAR measurements from different viewing geometries are available, one can solve for three deformation components [36,37]. In this study, we derived the LOS deformation velocities based on two independent InSAR passes; thus, only 2D velocity retrieval was possible.

Having LOS velocity estimates from ascending (V_{los_asc}) and descending (V_{los_desc}) passes coupled with satellite geometrical parameters, we started the first vector decomposition and retrieved deformation velocities in 2D—namely, vertical, V_v , and horizontal, V_h , velocities at individual QPS using [51] (cf. Figure 3):

$$\begin{bmatrix} V_{los_asc} \\ V_{los_desc} \end{bmatrix} = \begin{bmatrix} \cos \theta_{E_asc} & \sin \theta_{E_asc} / \cos \Delta\alpha \\ \cos \theta_{E_desc} & \sin \theta_{E_desc} \end{bmatrix} \begin{bmatrix} V_v \\ V_h \end{bmatrix} \quad (4)$$

where $\Delta\alpha$ denotes the difference between ascending and descending satellite headings. The linear equation shown in Equation (4) has no redundancy, and therefore, it is not possible to derive the estimation error. The parameters of interest at individual PS, V_v , and V_h can then be solved via linear equation system inversion.

The major vertical uplift trend in the AoI detectable by InSAR could be considered as a mixture of GIA and the seasonal deformation signal, hereafter, GIA-SS. We inferred the GIA-SS magnitude based on the literature [52] and the median of the decomposed vertical velocities. After major vertical-deformation-velocity removal, the residual vertical V_{v_res} and horizontal components V_h can be inversely modelled to obtain two residual LOS vectors, namely, $V_{los_asc_res}$ and $V_{los_desc_res}$ (cf. Equation (5)). These residual vectors act as inputs for the second vector decomposition. The potential slope-deformation velocity V_{slope} and the velocity perpendicular to the slope surface—hereafter, V_{perp} —are the main results of this step (cf. Equation (6) and Figure 4).

$$\begin{bmatrix} V_{los_asc_res} \\ V_{los_desc_res} \end{bmatrix} = \begin{bmatrix} \cos \theta_{asc} & \sin \theta_{asc} / \cos \Delta\alpha \\ \cos \theta_{desc} & \sin \theta_{desc} \end{bmatrix} \begin{bmatrix} V_{v_res} \\ V_h \end{bmatrix} \quad (5)$$

$$\begin{bmatrix} V_{los_asc_res} \\ V_{los_desc_res} \end{bmatrix} = \begin{bmatrix} \cos \theta_{P_asc} & \sin \theta_{P_asc} / \cos \Delta\alpha \\ \cos \theta_{P_desc} & \sin \theta_{P_desc} \end{bmatrix} \begin{bmatrix} V_{perp} \\ V_{slope} \end{bmatrix} \quad (6)$$

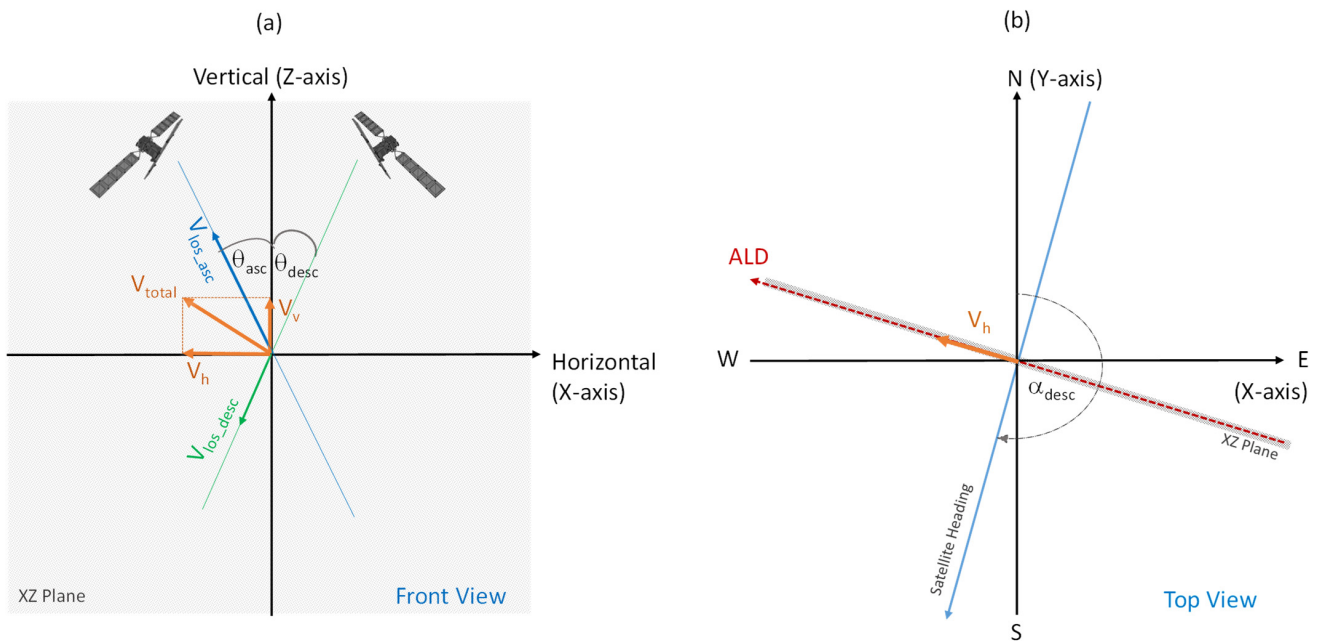


Figure 3. Schematic illustration of SAR imaging geometry: (a) front view (XZ plane) shows the V_{los_asc} vector (blue—moves toward the satellite) and the V_{los_desc} vector (green—moves away from the satellite) and the resulting V_{total} vector (moves up and westward, marked in orange). The V_{total} vector could be projected into its 2D components in vertical and horizontal directions, knowing the incidence angle (θ) and satellite heading (α); (b) SAR imaging geometry from top view (XY plane) illustrates descending satellite heading (α) and horizontal velocity vector (V_h) measurable using PSI in the Azimuth Look Direction (ALD).

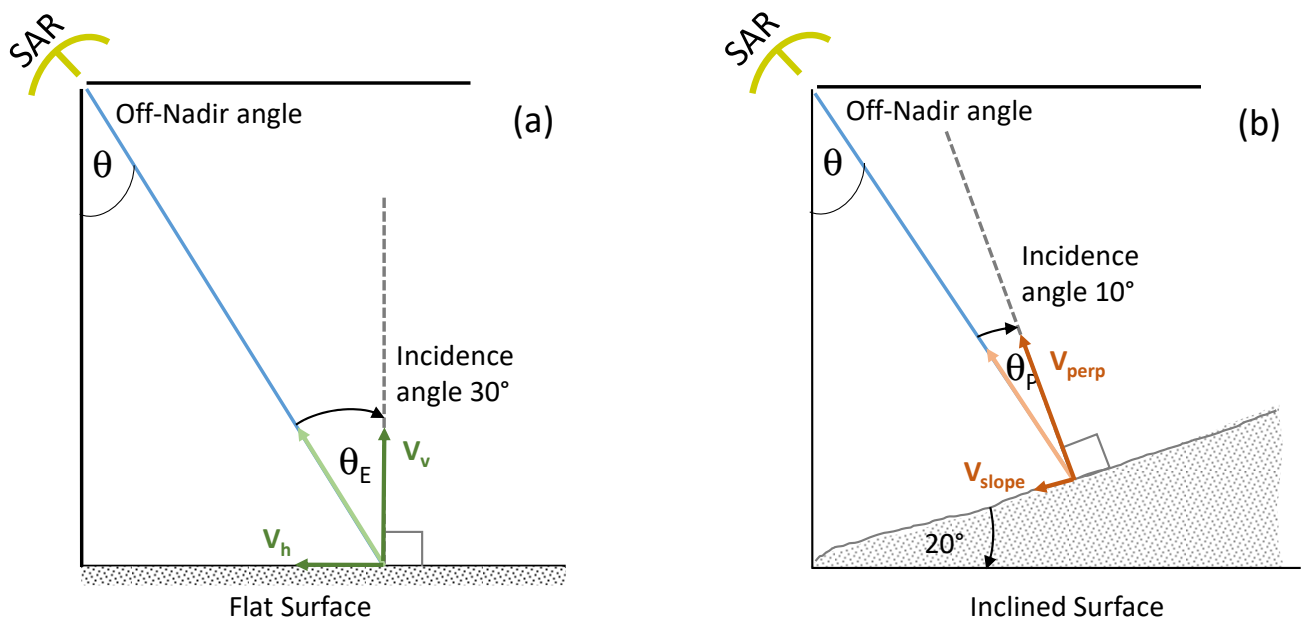


Figure 4. Graphical illustration of the nominal incidence angle (θ) and its changes when a radar sensor observes (a) a flat terrain and (b) the inclined slope (e.g., 20° slope gradients facing the sensor). In the latter case, the incidence angle decreases when the gradient of slope increases. The incidence angle in (a) depicts the concept of the Ellipsoid Incidence Angle (EIA, θ_E) which is normally used for LOS vector decomposition. The incidence angle in (b) represents the Projected Local Incidence Angle (PLIA, θ_P) we propose to use for decomposing V_{los} to V_{slope} in this study. The illustration also implies that while (a) EIA is SAR system-dependent and varies from near-range to far-range, (b) the PLIA is terrain-dependent.

2.3.3. Inferring the Local Deformation Fields Based on the PS-Based Estimates

Based on the reliable two-dimensional deformation estimates of QPSs and the MLV standard deviation, we further investigated their spatial distribution statistically, aiming to derive significant 2D deformation clusters. We then spatially analysed those deformation clusters based on two and three PS-based deformation parameters, resulting in nine and twenty-seven Unique Deformation Velocity (UDV) zones, respectively. To demonstrate the applicability of the detailed surface-deformation zoning results, we attempted to relate zonal attributes to possible deformation behaviours to interpret and better understand the motion processes that have taken place in the Öraefajökull area.

We recall the notion of previous studies stating that the magnitude of the GIA and the seasonal deformation signals in its vertical component (GIA-SS) are closely dependent on the distance to the ice caps and to the centre of Iceland [34,35]. Seasonal deformation is primarily contributed by glacial-mass balance and snow-load changes in glaciated and non-glaciated areas, respectively [53].

The Getis-Ord G_i^* Hot-Spot Analysis (HSA), as implemented in the ArcGIS spatial statistics tool [54], was applied to evaluate the spatial relationship between a pointwise estimate and its neighbourhood. HSA assesses the randomness of the value of a parameter, i.e., velocity at a point feature, in relation to its neighbouring points. Thus, significant clusters of high values (Hot Spot), low values (Cold Spot), or insignificant clusters (randomness is dominant) can be identified at different confidence levels (99%, 95%, and 90%), and meaningful movement patterns can be derived.

From the *spatial analysis (Combinatorial Or)* between the *std. V_{los}* and the 1D surface-movement rates, either the V_v or V_h parameter led to nine UDV zones in the AoI. Relying on the resulting unique zoning, we attempted to interpret the mixed deformation signals, i.e., the vertical component.

In practice, local surface-deformation zoning was achieved based on the following implementation steps:

- The Calculate Distance Band tool was used to initially investigate the neighbourhood of PS estimates, i.e., the relationship between the number of neighbouring PS points and the spatial distance between them was assessed. By inputting the expected number of neighbouring points, required for an arbitrary PS, the average, the minimum and the maximum distance bands were estimated. The average distance in which one obtains a sufficient number of PSs (>30), was then used for HSA.
- Hot-Spot Analysis was applied to evaluate the spatial distribution of three relevant deformation parameters (V_v , V_h , *std. V_{los}*) based on two spatial relationship concepts, the Inverse Distance Weighted (IDW) and the Fixed Distance Band (FDB), at different spatial scales. By increasing the FDB distance from 100, 250, and 500 to 1000 m, Hot-Spot and Cold-Spot clusters in the AoI, ranging from fine (local) to coarser scales, were mapped.
- The inputs for the spatial analysis were three rasterised deformation clusters from the HSA. To ensure high quality of the results, we selected three clusters (Hot Spot, Cold Spot, and not significant) with the highest confidence level (99%) of each parameter, resulting in nine distinct surface-deformation zones from each analysis.

3. Results

3.1. PS LOS Deformation-Rate Estimates

The resulting LOS deformation-rate estimates based on the PSI analysis are shown in Figure 5. The statistics are summarised in Table 2. A large number of PSs could be identified in both ascending (A) and descending (D) interferogram stacks, which correspond to a PS density of more than 450 PS/km²; this is comparable to dense urban areas. During 2015–2018, the median of relative LOS velocities (relative V_{los}) of both A and D data are slightly higher than zero (about +0.3 and +0.6 mm/y for A and D, respectively) with respect to the reference point (0 mm/y).

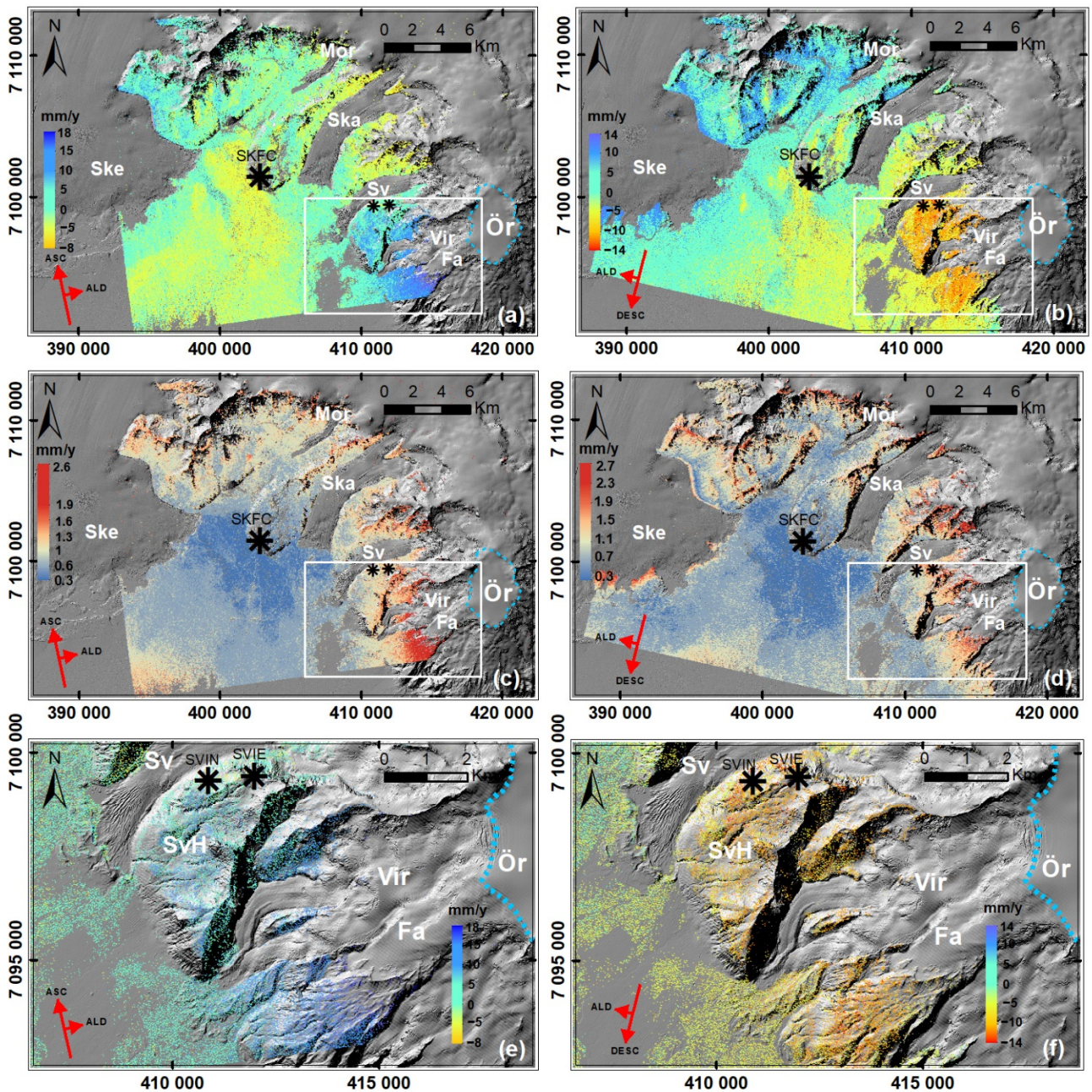


Figure 5. Relative Mean LOS Velocity (MLV or V_{los}) estimates, their standard deviation ($std. V_{los}$) and close-up of V_{los} estimates of Svínafellsheiði (SvH) slope in the left panel (a,c,e) from ascending data and the right panel (b,d,f) from descending orbit data. In (a,b,e,f), the cold colour tones (blue and cyan) illustrate PSs moving toward the satellite, and the warm colour tones (orange and red) represent PSs moving away from the satellite in the LOS direction. (c,d) represent $std. V_{los}$ obtained from PSI analysis with StaMPS. The Örafajökull (Ör) central volcano is marked in blue on the right side of the images. Abbreviations of major outlet glaciers and slope are presented in white from left to right: Ske—Skeiðarárjökull; Mor—Morsárjökull; Ska—Skaftafellsjökull; Sv—Svínafellsjökull; SvH—Svínafellsheiði slope; Vir—Virkisjökull; and Fa—Falljökull. The background image shows the AoI in shaded relief derived from the Arctic DEM.

Table 2. Statistical descriptions of relative and calibrated mean LOS velocity (V_{los}) estimates, with PS density obtained from PSI analysis of ascending (A) and descending (D) data.

Pass/Orbit	Master Scene (# of ifg)	Nr. of PS (PS/km ²)	Relative V_{los} (mm/y) Min. to Max. (Median)	Calibrated V_{los} Min. to Max. (Median)	<i>std.</i> V_{los} (mm/y) Min. to Max. (Median)
A118	27/08/2016 (28 ifgs)	214,061 (~460)	−8.1 to +17.9 (0.3)	10.3 to 36.3 (18.7)	0.3 to 2.6 (0.9)
D111	26/09/2016 (25 ifgs)	228,335 (~480)	−13.7 to +13.6 (0.6)	6.7 to 34.0 (21.1)	0.3 to 2.7 (1.0)

¹ standard deviation.

Calibrated V_{los} values of the GPS time-series at the SKFC reference point obtained from Equation (3) for the A and D data are 18.4 mm/y ($\theta = 44.3, \alpha = 350.6$) and 20.4 mm/y ($\theta = 39.8, \alpha = 191.0$), respectively. These absolute LOS velocities of SKFC were used to calibrate other estimates linearly, resulting in the calibrated velocity shown in Table 2. Note that the horizontal plate-spreading signal was preliminarily estimated and removed from 3D GPS measurements prior to the calibration. Therefore, our calibrated LOS velocity estimates do not contain deformation signals subjected to plate spreading.

The median values of uncertainties (*std.* V_{los}) of the LOS estimates are approximately 1 mm/y for both tracks. Precisely, ascending data have slightly lower *std.* V_{los} , which is likely due to the greater number of interferograms used in the PSI.

The initial visual interpretation of the relative LOS estimates of both A and D data in Figure 5a,b indicates that PSs with cold colour tones (light green to blue) have moved towards the satellite (positive velocity). PSs with warm colour tones (yellow to red) have moved away from the satellite (negative velocity) during this time span, relative to the reference point.

The interpretation also indicated remarkable areas with extreme colour differences—i.e., blue in A and orange in D data (Figure 5e,f), corresponding to positive and negative LOS velocities, respectively—observed on the slopes south of Svínafellsjökull and southwest of the Virkisjökull and Falljökull outlet glaciers (areas surrounded by white rectangle, cf. Figure 5). This occurrence can be explained using Figure 3a: when the ascending V_{los} is positive and descending V_{los} is negative, the horizontal component (V_h) of the resulting motion vector (V_{total}) should be significantly present during our observation period. However, when the horizontal component is not significant, the resulting LOS vectors projected between the two LOS vectors can be either positive or negative.

The standard deviation of LOS deformation-rate estimates (*std.* V_{los}) informs us about the degree of nonlinearity (NL) of the movement, i.e., how much an individual velocity (of an interferogram) deviated from the mean velocity during the observed period, expressed in mm/y. The larger the value, the more a PS has deformed nonlinearly with time. The estimated standard deviation ranges from 0.3 to 2.6 or 2.7 mm/y for our ascending and descending data. The *Std.* V_{los} estimates shown in Figure 5c,d indicate clearly that PSs located at the margin of the glaciers (orange/red points) deformed in a nonlinear fashion compared to PSs located further away from the glaciers.

Validation of PS LOS Deformation-Rate Estimates

Comparisons between the GPS LOS deformation and the calibrated LOS deformation time-series (hereafter, absolute LOS velocity— V_{los}) of the selected PSs surrounding three GPS stations (SKFC, SVIN, SVIE) over the SAR observation period are shown in Figure 6. The PS V_{los} estimate represented by the red lines in Figure 6a–f is the least square estimate of the LOS deformation velocities from all selected PSs (3–4 PSs per station). The GPS LOS deformation rate, represented by the black dotted lines in Figure 6a–f, was derived from the best available GPS time series. GPS measurement outliers were omitted during the GPS LOS velocity estimation. The uncertainties (s_N, s_E, s_U) of the GPS deformation time-series measurements are 2–3 mm for d_N , 2 mm for d_E , and 6–8 mm for d_U .

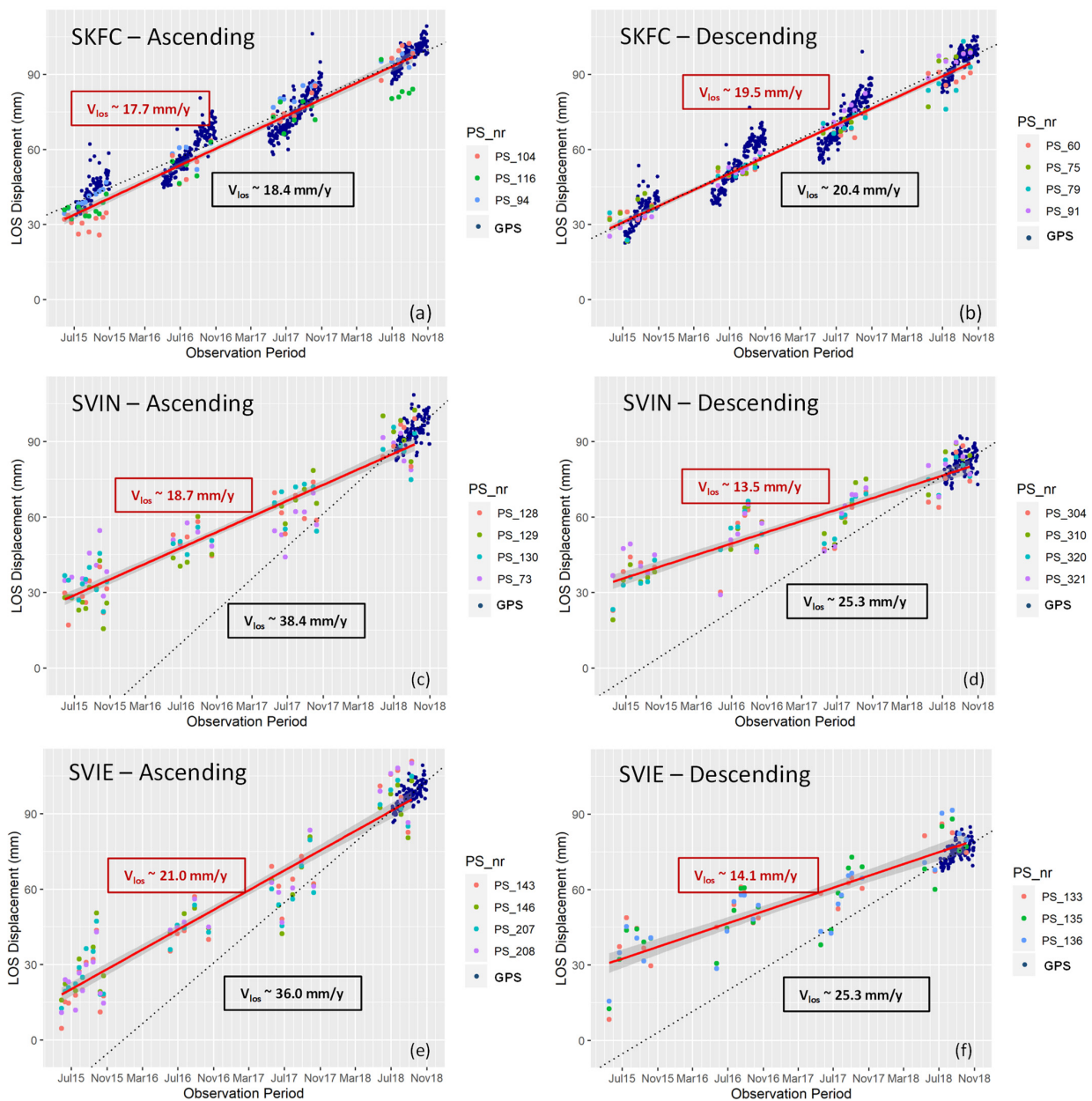


Figure 6. Validation of PS LOS deformation estimates (colourful dots) against independent GPS time-series measurements (dark blue dots) observed at three GPS reference points—(a,b) SKFC, (c,d) SVIN, and (e,f) SVIE—spanning the SAR time period from 2015 to 2018. The left panel figures show PS LOS deformation time-series and LOS deformation rates (red lines) derived from ascending data, and the right panel figures from descending data. The difference in the movement behaviours (degree of NL) between the reference point (SKFC) and a point of interest (e.g., SVIN, SVIE) contributes to the discrepancy between PS-based and GPS-based deformation-rate estimates, demonstrated in the difference in the slope gradients (red lines vs. black dotted lines in (c–f)).

A comparison of the results indicates lower PS LOS velocity estimates (flatter slope of the red line) than the reference GPS deformation velocity (black dotted line) at the SVIN and SVIE stations. One of the reasons for PS underestimation is the usage of the LOS velocity of the reference point (SKFC), averaged over 4 years for the overall LOS estimate calibration. Whether this value is an optimal calibration value depends on the similarity of the deformation behaviour of a particular location compared to the reference point. Additionally, the *std. V_{los}* values indicate that PSs in the vicinity of SKFC deformed more linearly with time (lower *std. V_{los}* value) than PSs near the SVIN and SVIE locations

(cf. *std. V_{los}* in Table 3). As such, the difference in *std. V_{los}* implies a difference in movement behaviours and is one of the factors affecting these deviations, ranging from approximately -10 to -20 mm/y, from the reference GPS *V_{los}* estimates.

Table 3. Summary of statistics of 3D GPS time-series measurements at three reference points available for the InSAR period, with comparison between GPS *V_{los}* and PS *V_{los}* (cf. Figure 6), and the standard deviations of the selected PS deformation estimates used for validation.

Station (# GPS Obs.)	GPS dN ¹ /sN ² (mm)	GPS dE/sE (mm)	GPS dU/sU (mm)	Data	GPS <i>V_{los}</i> ³ / PS <i>V_{los}</i>	<i>Std. V_{los}</i> ⁴ PS Min. Max. (mm/y)
SKFC (550)	−13.0/2.6	6.1/2.1	45.8/8.0	A	18.4/19.7	0.5–1.0
				D	20.4/19.5	0.4–1.1
SVIN (109)	−2.8/2.1	−2.4/1.8	9.3/6.8	A	38.4/18.7	1.1–1.4
				D	25.3/13.5	1.1–1.4
SVIE (107)	−3.0/2.0	−2.1/1.7	7.7/6.3	A	36.0/21.0	1.4–1.6
				D	25.3/14.1	1.6–1.8

¹ Mean of deformation measurements (d) in N, E, and U directions averaged over the GPS observation period; ² average one sigma uncertainty (s) of GPS measurements in N, E, and U directions of the same period; ³ derived GPS LOS deformation velocity using satellite geometries; and ⁴ range of *std. V_{los}* of the selected PSs visualised in Figure 6.

3.2. Two-Dimensional Decomposed Deformation Velocities

Applying quality criteria selection and layover-shadow-mask buffering to all *V_{los}* estimates from both A and D data resulted in about 7% of PSs being eliminated; the remaining 93% were considered quality PSs (QPSs). We also observed that isolated PSs on the glaciers were almost 100% removed (cf. Figure 7a–d). The selected thresholds proved to be feasible, since PS clusters on the slopes and at the edge of the glaciers remained, while isolated PSs on glaciers were eliminated.

With an average PS density of more than 350 QPS/km², and considering the spatial-proximity tests, we decided to use the shortest search radius of 100 m to achieve a reasonable computing time. For the selected search distance of 100 m, the average number of across-track PSs in the proximity is 17, and the minimum is 1 for A and D data (for details, cf. Table 4). This means that *V_v* and *V_h* can be estimated for all QPSs surrounded by at least one across-track PS.

Table 4. Statistics of vertical *V_v* and horizontal velocities *V_h*, *V_{v-res}*, *V_{perp}*, and *V_{slope}* as a result of the first and the second vector-based decompositions of A2D, D2A and a combination of both A2D and D2A (cf. Figures 7 and 8).

Dataset	QPS ² Density PS/km ²	# Across-Track ³ PSs Min. to Max. (Mean)	<i>V_v</i> Min. to Max. (Median) mm/y	<i>V_h</i> Min. to Max. (Median) mm/y
A2D	~396	1–47 (17)	−18.9 to 37.7 (26.7)	−15.2 to 10.5 (1.2)
D2A	~360	1–39 (17)	−17.2 to 37.1 (26.7)	−14.4 to 9.5 (1.0)
Combined ¹ 1st decomposition	~757		−17.2 to 37.7 (26.7)	−15.2 to 10.5 (1.1)
Combined (after GIA-SS removal)	~757		<i>V_{v-res}</i> −7.8 to 12.7 (1.7)	<i>V_h</i> −15.2 to 10.5 (1.1)
Combined 2nd decomposition	~757		<i>V_{perp}</i> −8.1 to 17.7 (1.8)	<i>V_{slope}</i> −15.3 to 10.6 (1.1)

¹ Combination of A2D and D2A point estimates; ² quality PS; ³ descending data are the across-track for ascending data and vice versa.

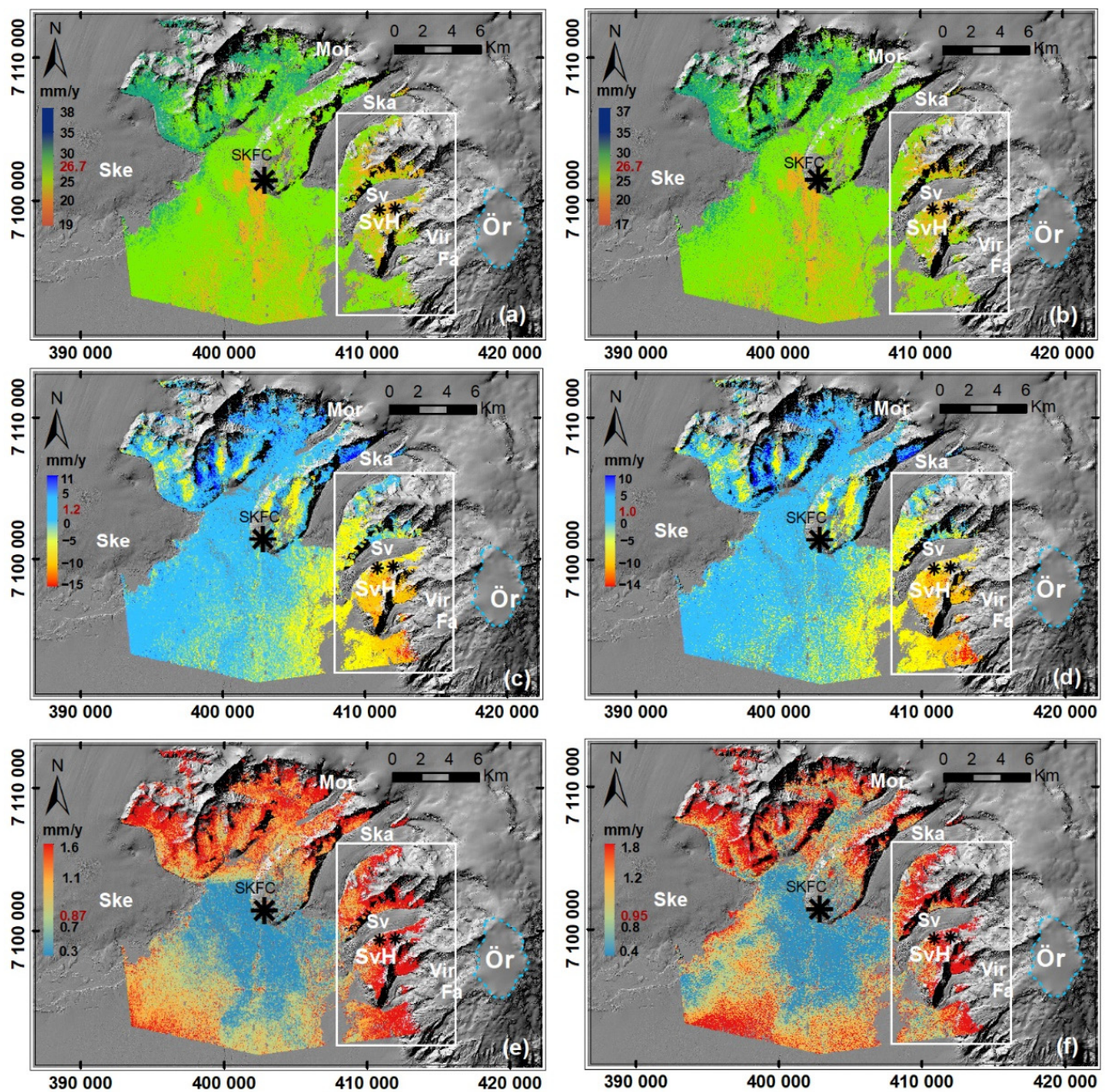


Figure 7. Decomposed deformation velocities in 2D: The left panel shows results from A2D decomposition, and the right panel shows results from D2A decomposition. (a,b) show the decomposed vertical velocities V_v ; (c,d) illustrate the decomposed horizontal velocities V_h ; and (e,f) show the range of the $std. V_{los}$ of the QPSs selected for the 2D decomposition from the ascending and descending data, respectively. Note that the maximum $std. V_{los}$ values of QPSs from A and D data decrease considerably (cf. Figure 5c,d), subjected to the removal of strongly nonlinear deforming PSs (high $std. V_{los}$) during the thresholding. Numbers in red for all colour scales indicate the median value of the presented parameter. White boxes in (a–f) indicate terrain slopes under primary investigation. Abbreviations of major outlet glaciers and slope are presented in white from left to right: Ske—Skeiðarárjökull; Mor—Morsárjökull; Ska—Skaftafellsjökull; Sv—Svínafellsjökull; SvH—Svínafellsheiði slope; Vir—Virkisjökull; and Fa—Falljökull. Öraefajökull (Ör) central volcano is circled by blue-dashed line.

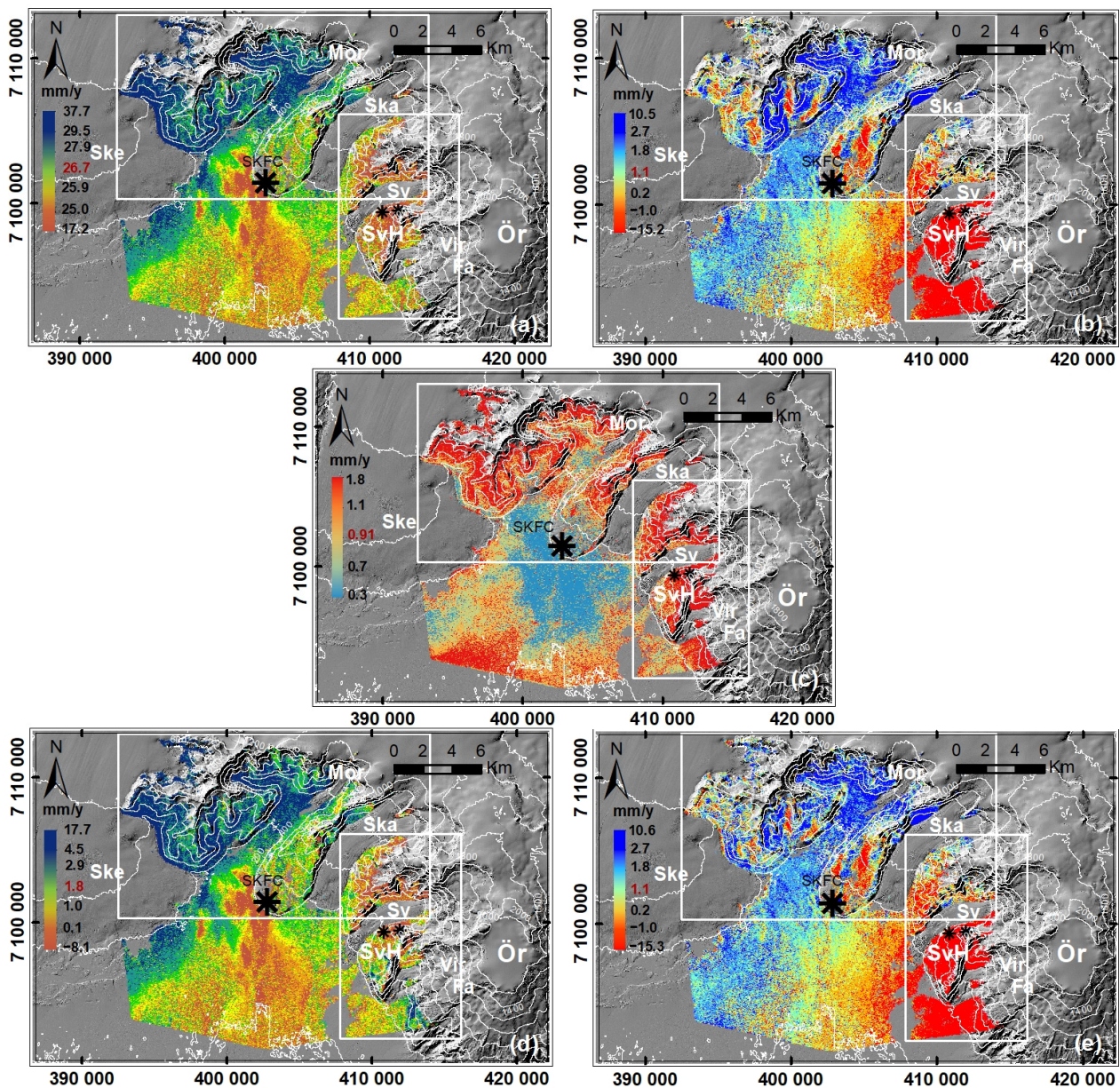


Figure 8. Combined vertical velocity V_v , horizontal velocity V_h , standard deviation V_{los} estimates, V_{perp} and V_{slope} from the A2D and D2A decompositions: (a) vertical velocities; (b) horizontal velocities resulting from the first vector decomposition; (c) $std. V_{los}$; (d) velocities perpendicular to the inclined surface V_{perp} ; and (e) slope-deformation velocities V_{slope} as a result of the second vector decomposition. The maximum vertical velocities are clustered on the mountain slopes between Skeiðarárjökull and Morsárjökull (upper white rectangle in (a–e)), parts of these slopes indicate strong movement towards the east direction (blue QPSs in (b)). Minimum vertical velocities are grouped into two clusters, i.e., on the slopes surrounding Svínafellsjökull and in low-lying areas lower than 200 m a.s.l. (brown QPSs in (a)). The lowest horizontal velocities are clustered on the south slope of Svínafellsjökull and southwest slopes of Virkisjökull and Falljökull outlet glaciers (lower white rectangle in (a–e) and red QPSs in (b)). The derivation of V_{perp} additionally reveals movements in the direction perpendicular to the slope surface at the Svínafellsheiði slope and the slope west of Virkisjökull and Falljökull, which were not detectable in the first decomposition (blue QPSs in (d)). Abbreviations of major outlet glaciers and slope are presented in white from left to right: Ske—Skeiðarárjökull; Mor—Morsárjökull; Ska—Skaftafellsjökull; Sv—Svínafellsjökull; SvH—Svínafellsheiði slope; Vir—Virkisjökull; Fa—Falljökull; and Ör—Öraefajökull central volcano.

The two-dimensional horizontal V_h and vertical velocity V_v as a result of the first V_{los} vector decomposition (cf. Equation (4)) are presented in Figure 7a–d. Our estimated V_v fields indicate lower vertical velocities at the Svínafellsheiði (SvH) slope and the slope south of Skaftafellsjökull compared to the slopes that lie between the Skeiðarárjökull and Skaftafellsjökull glaciers. The estimated V_h fields reveal that the entire Svínafellsheiði slope and the slope southwest of Virkisjökull and Falljökull predominantly displaced towards the west (negative V_h) at a magnitude of more than 10 mm/y (orange and red PSs). This supports our initial interpretation in Section 3.1 concerning the horizontal velocity. Other slopes (next to Skeiðarárjökull, Morsárjökull, and Skaftafellsjökull glaciers) indicate a mixture of horizontal movements that move partially towards the east or the west (blue or yellow, Figure 7c,d).

We applied quantile data classification to visualise the *std.* V_{los} (Figures 7e,f and 8), with the aim of assigning an equal number of QPSs to each class, represented by individual colours. The fourth quantile classification divides the total QPS into an equal number of PSs (approximately 25%). Likewise, the sixth quantile classification divides the total QPSs into approximately 16.7%. Thus, the median of the parameter of interest and extremely deforming QPSs with their corresponding values can be spatially located and determined. The *std.* V_{los} distribution patterns in (Figures 7e,f and 8c indicate that 25% of QPSs located in the low-lying areas deform more linearly (blue QPSs have a *std.* V_{los} ranges from ~0.3–0.8 mm/y), while 25% of QPSs along the margin of the glaciers (red QPSs) tend to deform nonlinearly (*std.* V_{los} higher than ~1.1 mm/y).

The A2D and D2A estimates were spatially combined, leading to almost double the number of robust measurement points (QPS density). The major vertical uplift trend, the GIA-SS, was inferred based on the median of the decomposed vertical velocities (median V_v 26.7 mm/y estimated from more than 350,000 PSs), from the literature [52], and from the fact that our calibrated LOS velocity at SKFC is an underestimate (cf. Figure 6). The constant rate of 25 mm/y was subtracted from V_v , resulting in V_{v_res} being used for the second decomposition.

The results in Figure 8 are visualised based on quantile data classification. Here, we divided V_v , V_h , V_{perp} , and V_{slope} into six classes (~16.7% QPS per class). Hence, we can constrain the most dynamic locations in terms of the maximum and minimum motion rates based on our estimates. These dynamic QPSs (blue or red coloured) constitute only a small part of the total QPSs (max. 16.7%). Figure 8a shows that approximately one-third of the QPSs in our AoI are dominated by high vertical velocities (dark blue and dark green QPSs). Another one-third of the QPSs are potentially affected by other deformation processes, dominated by their horizontal component, i.e., red and orange QPSs showing negative vertical velocities (Figure 8b). We found that the maximum vertical velocities are clustered on the mountain slopes between Skeiðarárjökull and Morsárjökull, and parts of these slopes also show strong movement in the east direction (upper white rectangle in Figure 8a,b). The minimum vertical velocities were grouped into two clusters: one on the slopes surrounding Svínafellsjökull and the other in the low-lying areas lower than 200 m a.s.l. The highest horizontal motion rates are clustered on the southwest slope of the Virkisjökull and Falljökull outlet glaciers and the south slope of Svínafellsjökull, indicating movement westward. Figure 8d,e illustrate V_{perp} and V_{slope} results, respectively, obtained from the second vector decomposition. The V_{slope} estimates are almost identical to the V_h estimates, since the horizontal component has not been adjusted after the first decomposition step and its magnitude is small (cf. Table 4). Only a constant GIA-SS velocity of 25 mm/y was removed from the vertical component, giving V_{v_res} as input for the second vector decomposition. The V_{perp} , estimated from the residual vertical velocities V_{v_res} and V_h , shown in Figure 8d, additionally revealed movements in the direction perpendicular to the slope surface (blue) at the Svínafellsheiði slope and the slope southwest of Virkisjökull and Falljökull, which were not detectable during the first vector decomposition (cf. Figure 8a).

3.3. Derived Two-Dimensional Local Deformation Fields

3.3.1. Hot-Spot Analysis (HSA) Results

Applying Hot-Spot Analysis to the PS-based deformation estimates resulted in the identified clusters of high values (“Hot Spot”, presented in red), clusters of low values (“Cold Spot”, presented in blue), as well as clusters of “not significant” values (presented in grey) in Figure 9. The IDW approach provides a smoother transition between “Hot Spot”, “Cold Spot”, and “not significant” clusters than the FDB. This is because the FDB does not consider PSs lying outside the defined distance band, whereas IDW does. We adapted HSA results based on FDB = 100 m for two reasons: (1) our V_v and V_h estimates are derived based on 100 m spatial proximity, and (2) results from “calculate distance band” indicate an average number of neighbouring QPSs of 48 at FDB = 100 m, which is statistically significant. HSA enables us to statistically classify our AoI into three sub-areas based on the deformation parameter under consideration (V_v or V_h or $std. V_{los}$). For example, the analysis results differentiate dynamic zones affected by uplift or subsidence from stable zones. Similarly, the HSA of $std. V_{los}$ allows us to differentiate highly nonlinear deforming areas from more linear deforming areas.

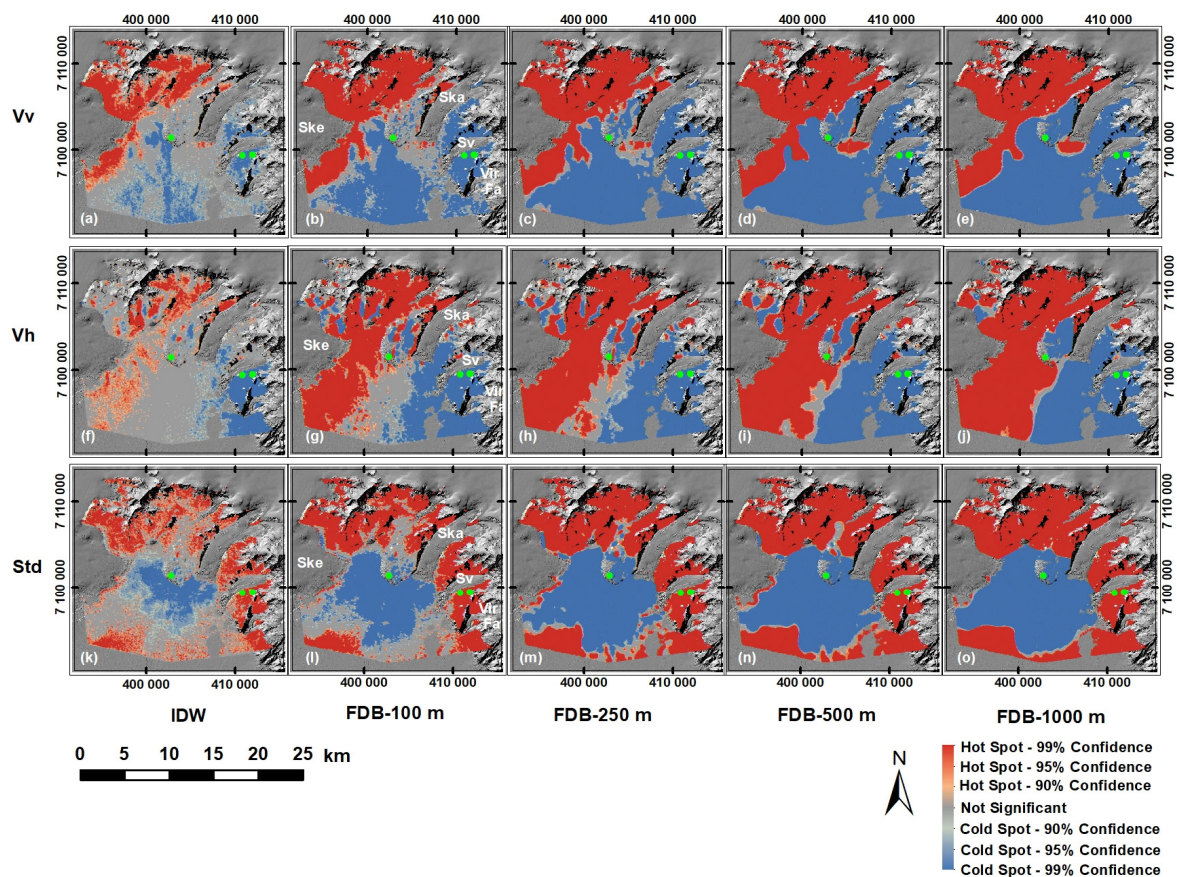


Figure 9. Hot Spots and Cold Spots identified based on two conceptual spatial relationships: Inverse Distance Weighted (IDW) and Fixed Distance Band (FDB). The IDW approach provides a smoother transition between “Hot Spot” (red), “Cold Spot” (blue), and “not significant” (grey) clusters than the FDB. Hot- and Cold-Spot clusters applying (a,f,k) IDW-100 m; (b,g,l) FDB-100 m; (c,h,m) FDB-250 m; (d,i,n) FDB-500 m; and (e,j,o) FDB-1000 m, for parameters V_v , V_h and $std. V_{los}$, respectively. When the FDB increases, the probability that a PS will be classified as Hot Spot (high value) or Cold Spot (low value) also increases, resulting in more homogenous clusters, as well as the gradual disappearance of insignificant clusters. The significant Hot-Spot and Cold-Spot clusters in (b,g,l) (FDB = 100 m) spatially outline the highly dynamic QPSs, implying that areas undergo extreme surface-deformation processes.

3.3.2. Interpretation of the Local Deformation Fields

Based on the HSA zones (100 m grid) with their mean velocities, we integrated the HSA results with two-dimensional pointwise estimates from PSI (~ 750 PS/km²), leading to spatially detailed surface-deformation velocity maps at the local scale, as shown in Figure 10. In Figure 10a–h, clusters with low values are outlined in blue, and clusters with high values are outlined in red.

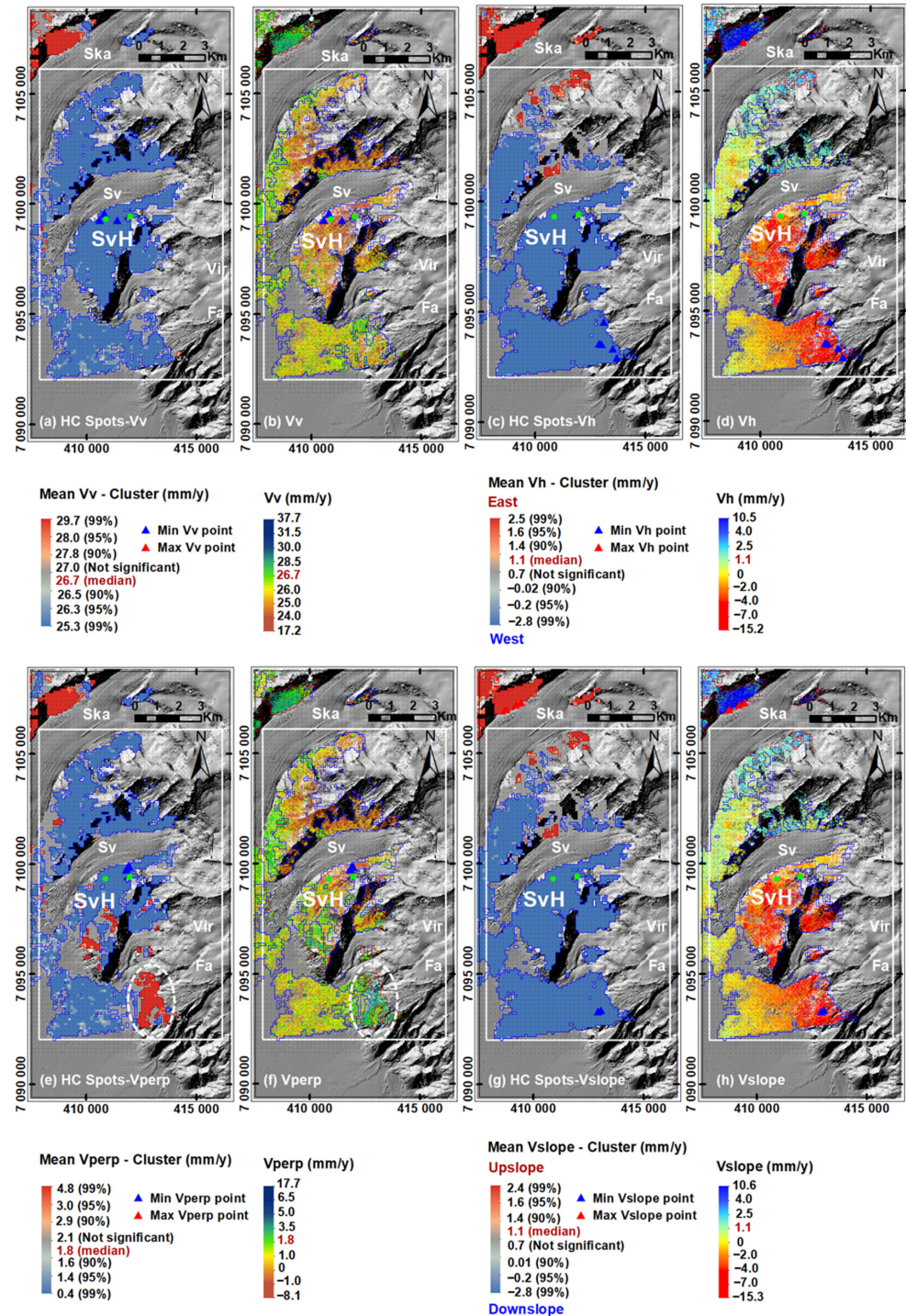


Figure 10. Visualisation of pairwise Hot-Spot and Cold-Spot clusters coupled with their one-dimensional PS-based deformation estimates of the terrain slopes around Svínafellsjökull: (a,b) Hot and Cold Spots of V_v and V_v ; (c,d) Hot and Cold Spots of V_h and V_h ; (e,f) Hot and Cold Spots of V_{perp} and V_{perp} ; and (g,h) Hot and Cold Spots of V_{slope} and V_{slope} . The red and blue triangles represent PS

points with the maximum and minimum values of the presented velocity parameters. The green circles represent the reference points (SVIN, SVIE). The mountain slopes as depicted from north to south are characterised by different 2D movement behaviours. Local deformation at the Svínafellsheiði slope (SvH) is more strongly dominated by horizontal surface-movement than the vertical movement during our study period (b,d). Deformation at the slope southward from Skaftafellsjökull is characterised by low V_v and by a partial mixture of horizontal movement towards the west and the east directions. The strongest horizontal movement in the AoI and relatively low vertical movement describe the deformation fields at the slope southwest of Virkisjökull and Falljökull. Abbreviations of major outlet glaciers and slope are presented in white from north to south: Ska—Skaftafellsjökull; Sv—Svínafellsjökull; SvH—Svínafellsheiði slope; Vir—Virkisjökull; and Fa—Falljökull.

The derived 2D deformation estimates resulting from the first vector decomposition indicate the minimum V_v (+17.2 mm/y) at the Svínafellsheiði slope and low V_v at the slope south of the Skaftafellsjökull, respectively (blue triangles and brown-shaded PSs in Figure 10b). PSs with the minimum V_h (−15.2 mm/y) and relatively low V_h were found at the slope southwest of the Virkisjökull and Falljökull glaciers and the Svínafellsheiði slope, respectively (blue triangles and orange-shaded PSs in Figure 10d). The obtained negative horizontal velocities at PSs indicate movement towards the off-west direction (Figure 10c,d), which agree well with independent GPS deformation observations at the SVIN and SVIE reference points in the area (cf. Table 3).

Two velocity components, V_{perp} and V_{slope} , were obtained from the second vector decomposition (Figure 10f,h). The terrain slope southwest of Virkisjökull and Falljökull shows low V_v (slightly higher than the assumed GIA-SS = 25 mm/y) and minimum horizontal movement (yellow–light-brown-shaded PSs in Figure 10b and blue triangles in Figure 10d, respectively). After removing the assumed GIA from V_v , the positive residual velocity remained, resulting in positive V_{perp} , and PSs differentiated themselves from the neighbourhood as Hot Spots (PS surrounded by white oval in Figure 10e,f). It should be noted that without applying the second decomposition, areas of different deformation behaviours, such as in this example, could not be detected.

The estimated two-dimensional deformation velocities from the second vector decomposition also suggest that the Svínafellsheiði terrain slope slightly moves perpendicular to the slope surface (mean V_{perp} +0.4 mm/y, Figure 10e) and in the downslope direction (min V_{slope} −2.8 mm/y, Figure 10g). During our observation period, the magnitude of the estimated horizontal movement in the off-west direction seems significant, as it suppresses the vertical component. Our results also indicate that surface deformation around Svínafellsheiði behaves differently compared to the mountain slopes east of Skeiðarárjökull, which move towards the off-east direction (lower white rectangle compared to the upper white rectangle in Figure 8d,e).

Spatial analysis of the rasterised velocity clusters (V_v and V_h) with $std. V_{los}$, as shown in Figure 9 leads to detailed categorisation of movement behaviours and the unique deformation velocity zones, characterised by different degrees of NL and movement directions in the AoI (cf. Figure 11).

Our results indicate a decrease in V_v from west to east of the AoI, i.e., changing from Hot Spot (mean V_v = 29.7 mm/y) to Cold Spot (mean V_v = 25.3 mm/y). This approximately corresponds to the increase in the distance from the centre of the ice cap (Figures 10a and 11b). The closer a PS is to the ice cap, the higher its V_v . An integrated interpretation of V_v and $std. V_{los}$ shows that PSs at higher altitudes deform more in the NL fashion than in low-lying areas (Figure 11b). Likewise, integrated interpretation of V_h and $std. V_{los}$ reveals that the areas lying approximately west of the Skaftafellsheiði slope deform towards the east, whereas areas to its east deform towards the west (Figure 11d). The PSs lying between 100 and 200 m a.s.l. do not indicate a significant horizontal movement pattern (cluster with random V_h , grey in Figure 11d).

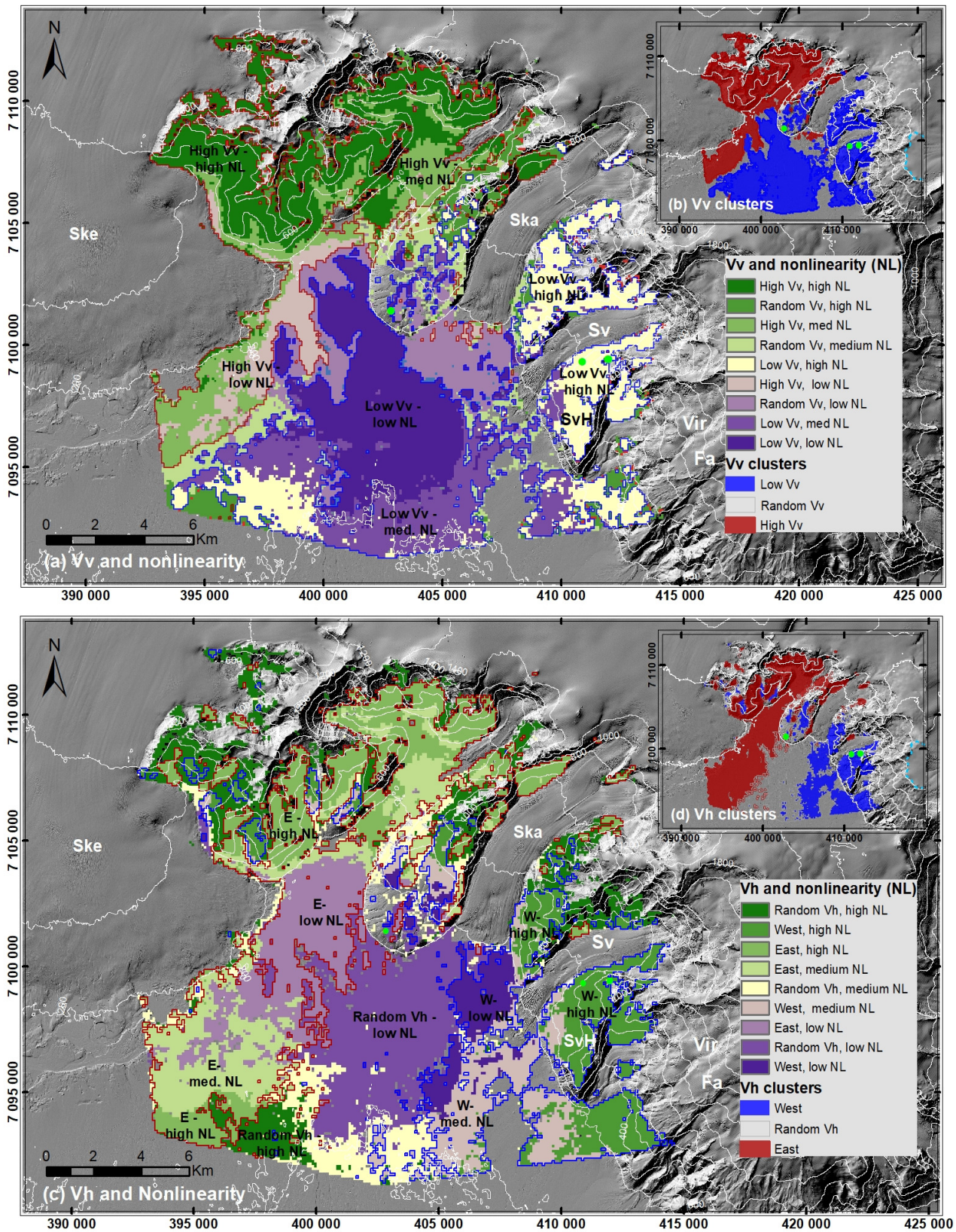


Figure 11. Two-dimensional local deformation velocity zoning as a result of spatial analysis based on two parameters: the velocity component (V_v or V_h) and the $std. V_{los}$. Each parameter is classified into three clusters, with high, medium, and low values, resulting in nine unique deformation velocity (UDV) zones. (a,c) show the V_v zones and the V_h zones, respectively; (b,d) insets illustrate V_v and V_h

high-value (Hot Spot), medium-value (insignificant/random), and low-value (Cold-Spot) clusters. Velocity zoning suggests, in (b), the deformation transition between the high and low V_v zones, and in (d), the transition between high and low V_h zones. Both transition zones lie approximately on the slope north of Skaftafellsjökull (Skaftafellsheiði slope). To the west of this transition zone, PSs deform with high V_v but different degrees of NL and move towards the east. To the east of the deformation transition zone, PSs indicate deformation towards the west with different degrees of nonlinearity. At Svínafellsheiði and the slope southwest of Virkisjökull and Falljökull, PSs indicate uniform, highly nonlinear surface deformation towards the west, but are characterised by low vertical velocity. Abbreviations of major outlet glaciers and slope are presented in white from left to right: Ske—Skeiðarárjökull; Ska—Skaftafellsjökull; Sv—Svínafellsjökull; SvH—Svínafellsheiði slope; Vir—Virkisjökull; and Fa—Falljökull.

Joint interpretation of the deformation attributes further shows that the mountain slopes north and south of Svínafellsjökull, including the terrain slope southwest of Virkisjökull and Falljökull, behave similarly (Figure 11a–d). Their deformation behaviours are characterised by low V_v , high NL, and horizontal movement towards the west, i.e., the cream-shaded areas in Figure 11a and the green-shaded areas in Figure 11c. Since the horizontal plate-spreading deformation was initially removed before the decomposition, the residual horizontal velocity, whose mean V_h ranges from +2.5 to 2.8 mm/y (Figures 10c and 11d), could be subjected to the horizontal component of seasonal deformation.

4. Discussion

MLV estimates derived from PSI analysis to quantitatively describe ongoing, two-dimensional deformation velocities in the Öræfajökull area show discrepancies ranging from ~2 to more than 10 mm/y when compared to independent GPS time-series measurements available for the same period (Figure 6). These deviations can be attributed to several factors. First, the use of the known velocity of the reference point (SKFC) to calibrate the relative PS LOS deformation-rate estimates globally led to underestimations of PS LOS velocities at SVIE and SVIN. The lower *std. V_{los}* value, which implies more linearity of the deformation of the reference point SKFC when compared to SVIE and SVIN, could be used to justify such discrepancies (cf. Figure 6c–f and Table 3). In addition, when the surface-deformation processes under consideration vary substantially in space and time, as in our case study, it is unlikely that an optimal calibrated velocity that fits all local deformation models can be found. This led to increasing deviations at PSs, where their deformation behaviours differ significantly from those of SKFC.

Second, only the 2018 annual GPS deformation rates of SVIN and SVIE were available for validation with the InSAR LOS velocity estimates, which have an acquisition time-span from 2015 to 2018. The difference in both measurement time spans could affect the validation accuracy. The obtained maximum uncertainty of QPS LOS estimates, or the standard deviation of the MLV, is approximately 2 mm/y.

Compared to previous studies that employed either 1D LOS displacement information [34] or 2D rasterised deformation estimates at a coarser scale for wide-area deformation mapping [35], we exploited the full potential of Sentinel-1 data for the derivation of 2D deformation estimates at full resolution based on a vector-based decomposition approach. Unlike raster-based algorithms, the applied workflow utilises LOS point estimates to derive 2D deformation velocities. The approach preserves the original point estimate accuracy and the subsequent 2D estimate accuracy as the processing errors are minimised. Rasterisation and interpolation of the velocity parameters were applied only in the final steps, spatial statistics and spatial analysis. With a PS density of 750 PS/km² and an average of 17 neighbouring QPSs (100 m search distance) used for the decomposition, our final product, the unique deformation velocity (UDV), represents the most detailed PS-based deformation zoning at its highest resolution and accuracy. For further quantitative assessment, the focal statistics of two-dimensional PS velocity estimates derived from A2D and D2A decompositions could be examined.

Our proposal to exploit the PLIA instead of the EIA in the two-step vector decomposition first allows for the isolation of deformation signals of interest. In our case, the assumed constant vertical deformation rate (GIA-SS) was subtracted, leaving the 2D residual components to be decomposed in the next step (Equation (5)). Second, the algorithm makes the direct derivation of V_{slope} and V_{perp} from 2D V_{los} measurements possible, which is particularly beneficial and unbiased for the derivation of surface-deformation information over both flat and inclined terrain. It should be noted that the V_h and V_{slope} value ranges are almost identical (Figure 8b,d). This is due to the fact that after the removal of the unwanted signals, plate spreading and GIA-SS, the magnitudes of the residual velocities are relatively small (Equation (6)).

Considering the challenges encountered in this study, such as the complex deformation signal in its vertical component, and the acquisition time of the SAR imagery analysed (May–October scenes), it is not possible to isolate the GIA from the semi-annual seasonal signal relying only on PSI. Since both signals were detected as uplift trends (positive V_v) during the observation period, we could only estimate the mixture of vertical deformation signals, i.e., the GIA-SS. In future, instead of removing the constant GIA-SS from the V_{los} before entering the second decomposition, possibilities for improving the GIA-SS spatial model, e.g., using *std. V_{los}* , should be investigated.

Integrated spatial analysis enables us to consider co-existing attributes based on two or three deformation parameters—i.e., V_v and *std. V_{los}* (Figure 11a); V_h and *std. V_{los}* (Figure 11c); and V_v , V_h and *std. V_{los}* (Figure 12b)—simultaneously. Depending on the number of parameters under consideration, two or three parameters, the analysis led to 9 to 27 UDV classes that describe the diversity of the geomorphological dynamics around Öraefajökull.

The combined interpretation of HSA results of *std. V_{los}* values and the elevation contours in Figure 12a indicates that PSs surrounded by a glacier or located at the margin of the outlet glaciers (red cluster) at higher altitudes (approximately 400 m–1000 m a.s.l.) deform more nonlinearly with time, with an average *std. V_{los}* value of ~ 1.2 mm/y. QPSs located further away from glaciers in low-lying areas (blue cluster, located between 100 m and 400 m a.s.l.) deform more linearly with time. The average *std. V_{los}* for this class is ~ 0.7 mm/y. QPSs with medium-nonlinearity deformation (grey cluster) have an average *std. V_{los}* of 0.9 mm/y. Using the fourth quantile classification for data visualisation further confirms that the high nonlinearly deforming (high NL) or linearly deforming (low NL) QPSs constitute smaller parts of the entire QPS, namely, 25% for each class (Figures 8c and 12a). The medium nonlinearly (medium NL) deforming QPSs comprise the largest part, i.e., 50% of the all QPSs. We can observe that on most of the mountain slopes, only PSs located below 1000 m a.s.l. could be detected in all of the interferograms and used for PSI, because these PSs were not covered by snow during the warmer months' SAR acquisitions. Based on this PS detectability finding, we propose 1000 m as the Equilibrium Line Altitude (ELA) for glaciers in the study area, which is consistent with the existing reference elevation [55]. In addition, we observed high *std. V_{los}* values (high NL) at QPSs located at high elevations (approximately 600–1000 m a.s.l.) when compared to the *std. V_{los}* of QPSs at lower altitudes (Figures 8c and 12a). This implies that QPSs located at higher altitudes, right below the ELA in the ablative zone, deform in a more nonlinear fashion than QPSs located at a lower altitude, further away from the ELA. If we assume the surface uplift due to GIA to be linearly constant over time, the nonlinear deformation component inferred from the *std. V_{los}* could be subjected to glacial-mass balance or snow-load changes, the main contribution to seasonal deformation in the area. Our findings are consistent with those of a previous study [53].

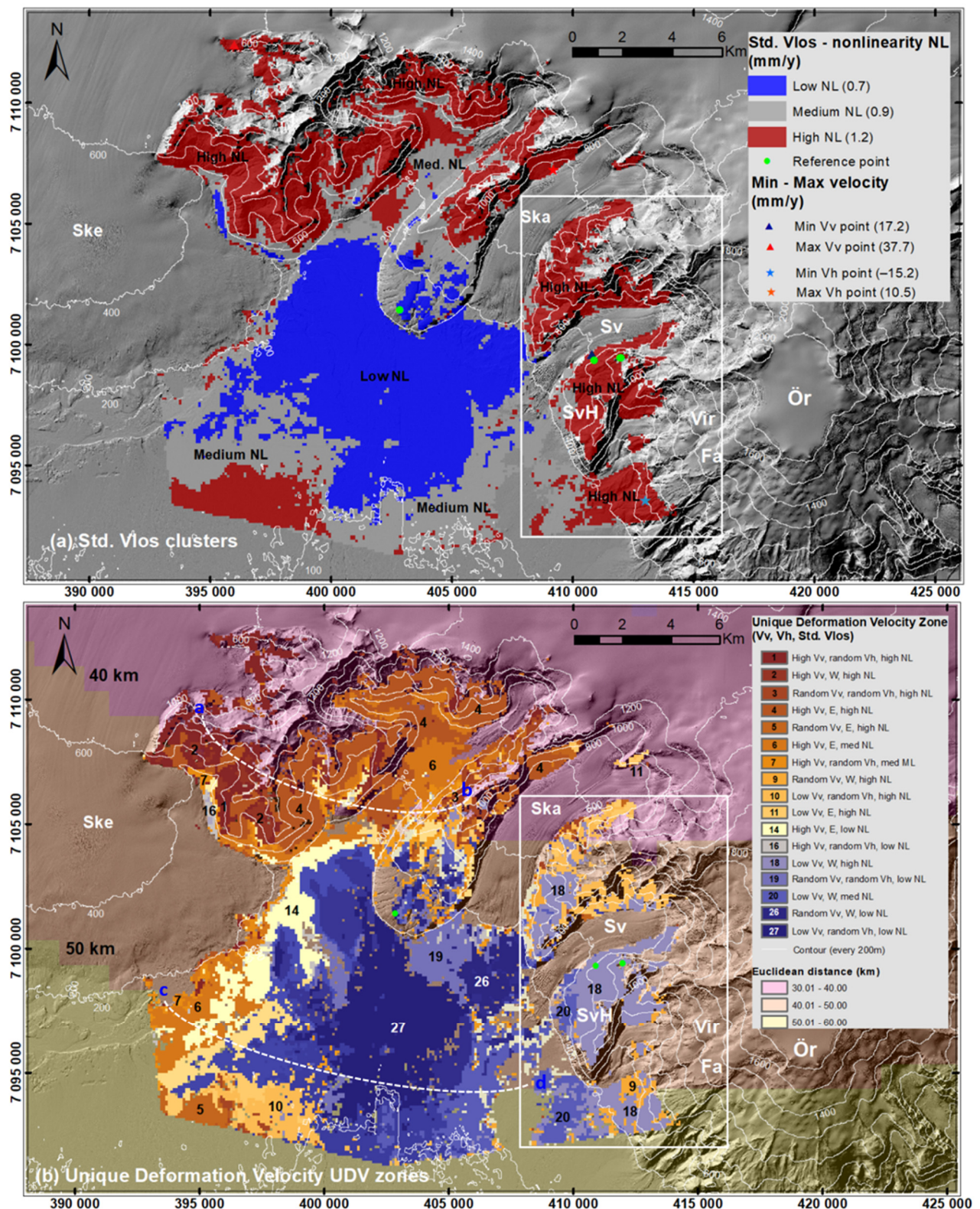


Figure 12. (a) Rasterised $std. V_{los}$ cluster as a result of HSA used to infer for surface-movement nonlinearity. PS points with estimated min and max 2D velocities are indicated; (b) twenty-seven detailed UDV zones derived based on the combined spatial analysis of three PS-based parameters (V_v , V_h and $std. V_{los}$) with the conceptual Euclidean distance measured approximately from the centre of Vatnajökull in the background. Our result shows that the Svínafellsheiði (SvH) slope and parts of the slopes located north and south of SvH (indicated by the white rectangle) are characterised by similar

deformation behaviours (zone 18). Its 2D deformation field is primarily dominated by horizontal motion towards the off-west direction and a small magnitude of vertical motion. The motion is also highly nonlinear. The UDV zoning result shows diversity of the two-dimensional local deformation patterns at the highest possible resolution. Abbreviations of major outlet glaciers and slope are presented in white from left to right: Ske—Skeiðarárjökull; Ska—Skaftafellsjökull; Sv—Svínafellsjökull; SvH—Svínafellsheiði slope; Vir—Virkisjökull; and Fa—Falljökull.

The combined interpretation of spatial analysis results provides detailed deformation information for Örafajökull as follows: First, we observed heterogeneous two-dimensional deformation patterns at the ends of glacier tongues at low elevations (e.g., 200 m a.s.l.). There is no indication of a specific movement pattern in either the vertical or horizontal component in these areas (random V_v and/or random V_h). Such heterogeneity can be observed at Skeiðarárjökull, Skaftafellsjökull, and Svínafellsjökull glacier termini (Figure 12b). Second, the V_v HSA clustering (Figure 11b) clearly defines the V_v transition zone located at the mountain slope northwest of Skaftafellsjökull. Likewise, the V_h HSA clustering (Figure 11d) indicates a V_h transition zone located at the same mountain slope. Localisation of the transition zone could be used to update the deformation inventory in the area.

Previous studies have suggested that the magnitude of GIA and the seasonal deformation signals (GIA-SS) are related to the distance to the Vatnajökull ice cap. Following this statement, the GIA-SS-induced V_v values of any arbitrary PSs located at the same Euclidean distance from the centre of Vatnajökull should be similar when only GIA-SS and no other coexisting deformation processes have taken place. Our investigations at points a and b, however, result in V_v magnitudes of 31.0 and 27.7 mm/y respectively (upper white dashed line in Figure 12b). Both points are located ~38 km away from the centre of Vatnajökull at approximately 800 m a.s.l. In addition, a larger V_v difference is observed between points c and d. The estimated V_v of point c is ~30.0 and of point d is ~25.3 mm/y, and they have the same Euclidean distance (50 km from Vatnajökull, cf. lower white dashed line in Figure 12b). Coupling V_v with the estimated V_h , we, therefore, interpret the overall 2D deformation field around point d (compared to point c) to be affected not only by the vertical motion (GIA-SS) but also by the more intense off-west horizontal motion. Likewise, the similar V_v magnitudes of points a and c, despite a Euclidean distance discrepancy of more than 10 km, cannot be satisfactorily explained by the aforementioned statement. In general, the 2D deformation fields around Örafajökull during our observation period were affected by diverse, coexisting deformation processes at both the regional and local scales. The regional vertical deformation signal (GIA-SS-like signal) is dominant in the west of the AoI. Moving to the east, closer to the Örafajökull volcano, the 2D deformation field is dominated by stronger horizontal motion, suppressing vertical motion.

5. Conclusions

In this study, we demonstrated the applicability of two-dimensional deformation estimates derived from the PSI of Sentinel-1 data, focusing on improved understanding of local deformation processes. Based on the vector-based LOS velocity decomposition approach, we derived high spatial resolution (PS density of 750 PS/km²) and more precise motion information (QPS LOS velocity uncertainty better than 2 mm/y) than those previously achieved by other geodetic measurements. The diversity and nonlinearity of the ground-surface-motion processes make direct exploitation of the absolute MLV estimate less effective. However, we demonstrate that by analysing QPSs' local spatial statistics (Hot Spot Analysis) in relation to their neighbours, statistically relevant QPSs can be grouped into meaningful clusters and used to describe local deformation trends, i.e., Hot Spots, Cold Spots, and not significant (random) clusters. The combined spatial analysis of three QPS-based parameters, V_v , V_h , and *std. V_{los}*, enables us to infer up to 27 UDV classes that characterise and reveal the diversity of the deformation behaviours around Örafajökull.

Our PS-based raster product, the UDV clusters, provides the most detailed (100 m grid) reliable deformation categorisation to date. The UDV zones provide us with more insight into the classification of ongoing deformation processes. We infer that local deformation fields west of Öräfajökull are dominated by high vertical motion in the west and by horizontal motion in the east. The approximate horizontal motion rate of -2.8 mm/y and low vertical motion rate of $+25.3$ mm/y describe the surface motion behaviours at Svínafellsheiði and the southwest slope of the Virkisjökull and Falljökull glaciers during the study period. Knowing the approximate location of V_v and V_h cluster boundaries and the mixture of random vertical and horizontal motion zones dominating at the north slope of Skaftafellsjökull, we infer this area to be the deformation transition zone.

For the first time, we introduce and demonstrate the results of a two-step vector decomposition that integrates the PLIA parameter in its implementation. We found that the concept is particularly beneficial for case studies where the isolation of two-dimensional deformation components is necessary and/or the surface motion of the inclined surface and slope-deformation rates are in focus.

In this study, we have demonstrated the potential use of the PS-based high-resolution 2D deformation products derived from the proposed workflow for improving the characterisation of the local deformation fields, determining the motion transitioning zone, and confirming the glacial ELA. Although the pointwise accuracy of the 2D PS estimate derived from this study is not as high as that of the geodetic measurement, PSI analysis of Sentinel-1 data has proved to be one of the most applicable techniques for the derivation of highly precise, two-dimensional surface-deformation information, complementary to traditional cost and time-intensive techniques.

Author Contributions: Conceptualisation, J.D. and D.H.; methodology, J.D.; software, J.D.; validation, J.D.; formal analysis, J.D.; investigation, J.D., D.H. and P.S.; writing—original draft preparation, J.D.; writing—review and editing, J.D., D.H., D.T. and P.S.; visualisation, J.D.; supervision, D.H.; project administration, D.H. and D.T.; funding acquisition, D.H. and D.T. All authors have read and agreed to the published version of the manuscript.

Funding: This research was funded by the Austrian Science Fund (FWF) through the project MORPH (Mapping, monitoring and modelling the spatio-temporal dynamics of land surface morphology; FWF-P29461-N29). Open Access Funding by the Austrian Science Fund (FWF).

Data Availability Statement: Not applicable.

Acknowledgments: The research team cordially thanks Benedikt G. Ófeigsson from the Icelandic Meteorological Office (IMO) for providing technical information and consultation on the 3D GPS time-series data used for validation purposes, and the German Aerospace Center (DLR) for granting the use of the TerraSAR-X datasets (under proposal nr. GEO3590) in the comparative study to Sentinel-1 data.

Conflicts of Interest: The authors declare no conflict of interest.

Appendix A. Decomposition Sensitivity

Recall Equation (3) from page 7:

$$v_{los} = \begin{bmatrix} -\sin \theta \cos \alpha & \sin \theta \sin \alpha & \cos \theta \end{bmatrix} \begin{bmatrix} v_E \\ v_N \\ v_U \end{bmatrix},$$

$[-\sin \theta \cos \alpha \quad \sin \theta \sin \alpha \quad \cos \theta]$ is the 3D component $[u_E \ u_N \ u_U]$ of the LOS unit vector with the direction pointing from the radar target (ground) to the satellite [56]. It can be used to describe the 3D decomposition sensitivity of InSAR LOS measurements. For example, Sentinel-1, which observes the Earth surface at an incidence angle of $\sim 38^\circ$ (approximately mid-range) and with a satellite heading of $\sim 191^\circ$ (descending), has a unit vector of $\sim [0.60 \quad -0.12 \quad 0.79]$. This means that from 100% of Sentinel-1 LOS deformation measurement, about 60% will be decomposed as the East–West, 12% as the North–South and

79% as the Up–Down components, respectively. Sensitivity to movements in the N–S direction is generally minimal, resulting from the near-polar orbit configuration of SAR systems [3,57]. Table A1 provides information about the decomposition sensitivity of selected SAR missions in comparison with Sentinel-1 for 3D deformation retrieval.

Table A1. Comparison of decomposition sensitivity (unit vector) for the InSAR LOS estimate from former and current SAR missions (cf. Equation (2) or (3)). All values are estimated at mid-swath incidence angle.

Mission	Incidence Angle (Mid-Range)	East (E)	North (N)	Up (U)
Sentinel-1 (A)	37°	−0.58	−0.16	0.80
Sentinel-1 (D)	37°	0.59	−0.10	0.80
Sentinel-1 (A) ¹	43.4°	−0.68	−0.11	0.73
Sentinel-1 (D) ²	38.7°	0.61	−0.12	0.78
TerraSAR-X (D)	32°	0.53	−0.05	0.85
ERS-1/2 (D)	23°	0.37	−0.14	0.92

^{1,2} parameters from Öræfajökull image subset analysed in this case study.

References

- Gabriel, A.K.; Goldstein, R.M.; Zebker, H.A. Mapping small elevation changes over large areas: Differential radar interferometry. *J. Geophys. Res.* **1989**, *94*, 9183–9191. [[CrossRef](#)]
- Ferretti, A.; Prati, C.; Rocca, F. Permanent scatterers in SAR interferometry. *IEEE Trans. Geosci. Remote Sens.* **2001**, *39*, 8–20. [[CrossRef](#)]
- Colesanti, C.; Wasowski, J. Investigating landslides with space-borne Synthetic Aperture Radar (SAR) interferometry. *Eng. Geol.* **2006**, *88*, 173–199. [[CrossRef](#)]
- Ferretti, A.; Prati, C.; Borghi, A.; Novali, F.; Savio, G.; Musazzi, S.; Barzaghi, R.; Rocca, F. Submillimeter Accuracy of InSAR Time Series: Experimental Validation. *IEEE Trans. Geosci. Remote Sens.* **2007**, *45*, 1142–1153. [[CrossRef](#)]
- Hooper, A.; Segall, P.; Zebker, H. Persistent scatterer interferometric synthetic aperture radar for crustal deformation analysis, with application to Volcán Alcedo, Galápagos. *J. Geophys. Res. Solid Earth* **2007**, *112*, 1–21. [[CrossRef](#)]
- Atzori, S.; Antonioli, A.; Tolomei, C.; de Novellis, V.; de Luca, C.; Monterroso, F. InSAR full-resolution analysis of the 2017–2018 $M > 6$ earthquakes in Mexico. *Remote Sens. Environ.* **2019**, *234*, 111461. [[CrossRef](#)]
- Albino, F.; Biggs, J.; Yu, C.; Li, Z. Automated Methods for Detecting Volcanic Deformation Using Sentinel-1 InSAR Time Series Illustrated by the 2017–2018 Unrest at Agung, Indonesia. *J. Geophys. Res. Solid Earth* **2020**, *125*, e2019JB017908. [[CrossRef](#)]
- Colesanti, C.; Ferretti, A.; Prati, C.; Rocca, F. Monitoring landslides and tectonic motions with the Permanent Scatterers Technique. *Eng. Geol.* **2003**, *68*, 3–14. [[CrossRef](#)]
- Bovenga, F.; Nitti, D.O.; Fornaro, G.; Radicioni, F.; Stoppini, A.; Brigante, R. Using C/X-band SAR interferometry and GNSS measurements for the Assisi landslide analysis. *Int. J. Remote Sens.* **2013**, *34*, 4083–4104. [[CrossRef](#)]
- Intrieri, E.; Raspini, F.; Fumagalli, A.; Lu, P.; del Conte, S.; Farina, P.; Allievi, J.; Ferretti, A.; Casagli, N. The Maoxian landslide as seen from space: Detecting precursors of failure with Sentinel-1 data. *Landslides* **2018**, *15*, 123–133. [[CrossRef](#)]
- Lauknes, T.R.; Piyush Shanker, A.; Dehls, J.F.; Zebker, H.A.; Henderson, I.H.C.; Larsen, Y. Detailed rockslide mapping in northern Norway with small baseline and persistent scatterer interferometric SAR time series methods. *Remote Sens. Environ.* **2010**, *114*, 2097–2109. [[CrossRef](#)]
- Worawattanamateekul, J.; Hoffmann, J.; Bamler, R.; Altermann, W.; Kampes, B.; Adam, N.; Roth, A. Derivation of Surface Subsidence Information in Bangkok (Thailand) by PS Analysis of a Limited Number of Interferograms. In Proceedings of the Fringe Workshop, Frascati, Italy, 28 November–2 December 2005.
- Yu, L.; Yang, T.; Zhao, Q.; Liu, M.; Pepe, A. The 2015–2016 ground displacements of the Shanghai coastal area inferred from a combined COSMO-SkyMed/Sentinel-1 DInSAR analysis. *Remote Sens.* **2017**, *9*, 1194. [[CrossRef](#)]
- Carlà, T.; Farina, P.; Intrieri, E.; Ketizmen, H.; Casagli, N. Integration of ground-based radar and satellite InSAR data for the analysis of an unexpected slope failure in an open-pit mine. *Eng. Geol.* **2018**, *235*, 39–52. [[CrossRef](#)]
- Ferretti, A.; Prati, C.; Rocca, F. Nonlinear subsidence rate estimation using permanent scatterers in differential SAR interferometry. *IEEE Trans. Geosci. Remote Sens.* **2000**, *38*, 2202–2212. [[CrossRef](#)]
- Bamler, R.; Eineder, M.; Adam, N.; Zhu, X.; Gernhardt, S. Interferometric potential of high resolution spaceborne SAR. *Photogramm. Fernerkund. Geoinf.* **2009**, *2009*, 407–419. [[CrossRef](#)]
- Crosetto, M.; Monserrat, O.; Cuevas-González, M.; Devanathéry, N.; Luzi, G.; Crippa, B. Measuring thermal expansion using X-band persistent scatterer interferometry. *ISPRS J. Photogramm. Remote Sens.* **2015**, *100*, 84–91. [[CrossRef](#)]

18. Dong, J.; Zhang, L.; Tang, M.; Liao, M.; Xu, Q.; Gong, J.; Ao, M. Mapping landslide surface displacements with time series SAR interferometry by combining persistent and distributed scatterers: A case study of Jiaju landslide in Danba, China. *Remote Sens. Environ.* **2018**, *205*, 180–198. [CrossRef]
19. ESA—Sentinel-1 Operations. Available online: https://www.esa.int/Enabling_Support/Operations/Sentinel-1_operations (accessed on 26 July 2021).
20. Sentinel-1—Missions—Sentinel Online—Sentinel Online. Available online: <https://sentinels.copernicus.eu/web/sentinel/missions/sentinel-1> (accessed on 26 July 2021).
21. SNAP—STEP. Available online: <https://step.esa.int/main/toolboxes/snap/> (accessed on 26 July 2021).
22. Veci, L.; Prats-Iraola, P.; Scheiber, R.; Collard, F.; Fomferra, N.; Engdahl, M. The Sentinel-1 Toolbox. In Proceedings of the IEEE International Geoscience and Remote Sensing Symposium (IGARSS), Québec, QC, Canada, 13–18 July 2014; pp. 1–3.
23. Wasowski, J.; Bovenga, F. Investigating landslides and unstable slopes with satellite Multi Temporal Interferometry: Current issues and future perspectives. *Eng. Geol.* **2014**, *174*, 103–138. [CrossRef]
24. Bianchini, S.; Cigna, F.; Righini, G.; Proietti, C.; Casagli, N. Landslide HotSpot Mapping by means of Persistent Scatterer Interferometry. *Environ. Earth Sci.* **2012**, *67*, 1155–1172. [CrossRef]
25. Solari, L.; Del Soldato, M.; Montalti, R.; Bianchini, S.; Raspini, F.; Thuegaz, P.; Bertolo, D.; Tofani, V.; Casagli, N. A Sentinel-1 based hot-spot analysis: Landslide mapping in north-western Italy. *Int. J. Remote Sens.* **2019**, *40*, 7898–7921. [CrossRef]
26. Confuorto, P.; Di Martire, D.; Centolanza, G.; Iglesias, R.; Mallorqui, J.J.; Novellino, A.; Plank, S.; Ramondini, M.; Thuro, K.; Calcaterra, D. Post-failure evolution analysis of a rainfall-triggered landslide by multi-temporal interferometry SAR approaches integrated with geotechnical analysis. *Remote Sens. Environ.* **2017**, *188*, 51–72. [CrossRef]
27. Lu, P.; Casagli, N.; Catani, F.; Tofani, V. Persistent scatterers interferometry hotspot and cluster analysis (PSI-HCA) for detection of extremely slow-moving landslides. *Int. J. Remote Sens.* **2012**, *33*, 466–489. [CrossRef]
28. Dai, K.; Li, Z.; Tomás, R.; Liu, G.; Yu, B.; Wang, X.; Cheng, H.; Chen, J.; Stockamp, J. Monitoring activity at the Daguangbao mega-landslide (China) using Sentinel-1 TOPS time series interferometry. *Remote Sens. Environ.* **2016**, *186*, 501–513. [CrossRef]
29. Carlà, T.; Intrieri, E.; Raspini, F.; Bardi, F.; Farina, P.; Ferretti, A.; Colombo, D.; Novali, F.; Casagli, N. Perspectives on the prediction of catastrophic slope failures from satellite InSAR. *Sci. Rep.* **2019**, *9*, 14137. [CrossRef]
30. Adam, N.; Kampes, B.M.; Eineder, M.; Worawattanamateekul, J.; Kircher, M. The development of a scientific permanent scatterer system. In Proceedings of the Joint ISPRS/EARSeL Workshop “High Resolution Mapping from Space”, Hannover, Germany, 6–8 October 2003.
31. Kampes, B.M. *Radar Interferometry Persistent Scatterer Technique*; Springer: Dordrecht, The Netherlands, 2006; ISBN 9781402045769.
32. Hooper, A. A multi-temporal InSAR method incorporating both persistent scatterer and small baseline approaches. *Geophys. Res. Lett.* **2008**, *35*, 1–5. [CrossRef]
33. Árnadóttir, T.; Lund, B.; Jiang, W.; Geirsson, H.; Björnsson, H.; Einarsson, P.; Sigurdsson, T. Glacial rebound and plate spreading: Results from the first countrywide GPS observations in Iceland. *Geophys. J. Int.* **2009**, *177*, 691–716. [CrossRef]
34. Auriac, A.; Spaans, K.H.; Sigmundsson, F.; Hooper, A.; Schmidt, P.; Lund, B. Iceland rising: Solid Earth response to ice retreat inferred from satellite radar interferometry and viscoelastic modeling. *J. Geophys. Res. Solid Earth* **2013**, *118*, 1331–1344. [CrossRef]
35. Drouin, V.; Sigmundsson, F. Countrywide Observations of Plate Spreading and Glacial Isostatic Adjustment in Iceland Inferred by Sentinel-1 Radar Interferometry, 2015–2018. *Geophys. Res. Lett.* **2019**, *46*, 8046–8055. [CrossRef]
36. Rocca, F. 3D motion recovery with multi-angle and/or left right interferometry. In Proceedings of the Fringe 2003 Workshop, Frascati, Italy, 1–5 December 2003.
37. Wright, T.J. Toward mapping surface deformation in three dimensions using InSAR. *Geophys. Res. Lett.* **2004**, *31*, L01607. [CrossRef]
38. Helgason, J.; Duncan, R.A. Stratigraphy, 40Ar-39Ar dating and erosional history of Svínafell, SE Iceland. *Jökull* **2013**, *63*, 33–53.
39. Sæmundsson, Þ.; Sigurðsson, I.A.; Pétursson, H.G.; Jónsson, H.P.; Decaulne, A.; Roberts, M.J.; Jensen, E.H. Bergflóðið sem féll á Morsárjökul 20. mars 2007—Hverjar hafa afleiðingar þess orðið? *Náttúrufræðingurinn* **2011**, *81*, 131–141.
40. Ben-Yehoshua, D.; Sæmundsson, Þ.; Helgason, J.K.; Belart, J.M.C.; Sigurðsson, J.V.; Erlingsson, S. Paraglacial exposure and collapse of glacial sediment: The 2013 landslide onto Svínafellsjökull, southeast Iceland. *Earth Surf. Process. Landf.* **2022**. [CrossRef]
41. Sigmundsson, F.; Einarsson, P.; Hjartardóttir, Á.R.; Drouin, V.; Jónsdóttir, K.; Árnadóttir, T.; Geirsson, H.; Hreinsdóttir, S.; Li, S.; Ófeigsson, B.G. Geodynamics of Iceland and the signatures of plate spreading. *J. Volcanol. Geotherm. Res.* **2018**, *391*, 106436. [CrossRef]
42. ArcticDEM—Polar Geospatial Center. Available online: <https://www.pgc.umn.edu/data/arcticdem/> (accessed on 27 July 2021).
43. German Aerospace Center. *DEM Products Specification Document (Doc: TD-GS-PS-0021)*; Issue 3.0; German Aerospace Center: Wessling, Germany, 2013.
44. de Zan, F.; Guarnieri, A.M. TOPSAR: Terrain observation by progressive scans. *IEEE Trans. Geosci. Remote Sens.* **2006**, *44*, 2352–2360. [CrossRef]
45. Fomelis, M.; Blasco, J.M.D.; Desnos, Y.L.; Engdahl, M.; Fernández, D.; Veci, L.; Lu, J.; Wong, C. ESA SNAP—Stamps integrated processing for Sentinel-1 persistent scatterer interferometry. In Proceedings of the International Geoscience and Remote Sensing Symposium (IGARSS), Valencia, Spain, 22–27 July 2018; Volume 2018.
46. Hooper, A.; Bekaert, D.; Spaans, K.; Arikan, M. Recent advances in SAR interferometry time series analysis for measuring crustal deformation. *Tectonophysics* **2012**, *514–517*, 1–13. [CrossRef]

47. Hooper, A.; Spaans, K.; Bekaert, D.; Cuenca, M.C.; Arkan, M. StaMPS/MTI Manual Version 4.1b. 2018, p. 44. Available online: <https://docplayer.net/94667136-Stamps-mti-manual-version-4-1b-andy-hooper-david-bekaert-ekbal-hussain-and-karsten-spaans-15th-august-2018.html> (accessed on 5 April 2022).
48. Fomelis, M. Vector-based approach for combining ascending and descending persistent scatterers interferometric point measurements. *Geocarto Int.* **2018**, *33*, 38–52. [[CrossRef](#)]
49. Hanssen, R.F. *Radar Interferometry: Data Interpretation and Error Analysis*; Kluwer Academic Publishers: Dordrecht, The Netherlands, 2001; ISBN 0-7923-6945-9.
50. Fuhrmann, T.; Garthwaite, M.C. Resolving three-dimensional surface motion with InSAR: Constraints from multi-geometry data fusion. *Remote Sens.* **2019**, *11*, 241. [[CrossRef](#)]
51. Blasco, J.M.D.; Fomelis, M.; Stewart, C.; Hooper, A. Measuring urban subsidence in the Rome Metropolitan Area (Italy) with Sentinel-1 SNAP-StaMPS Persistent Scatterer Interferometry. *Remote Sens.* **2019**, *11*, 129. [[CrossRef](#)]
52. Sigmundsson, F.; Parks, M.; Pedersen, R.; Jónsdóttir, K.; Ófeigsson, B.G.; Grapenthin, R.; Dumont, S.; Einarsson, P.; Drouin, V.; Rafn Heimisson, E.; et al. Magma movements in volcanic plumbing systems and their associated ground deformation and seismic patterns. In *Volcanic and Igneous Plumbing Systems: Understanding Magma Transport, Storage, and Evolution in the Earth's Crust*; Elsevier Inc.: Amsterdam, The Netherlands, 2018; pp. 285–322. ISBN 9780128097496.
53. Drouin, V.; Heki, K.; Sigmundsson, F.; Hreinsdóttir, S.; Ófeigsson, B.G. Constraints on seasonal load variations and regional rigidity from continuous GPS measurements in Iceland, 1997–2014. *Geophys. J. Int.* **2016**, *205*, 1843–1858. [[CrossRef](#)]
54. ArcGIS Desktop 10.7.1 Quick Start Guide—ArcMap | Documentation. Available online: <https://desktop.arcgis.com/en/arcmap/10.7/get-started/setup/arcgis-desktop-quick-start-guide.htm> (accessed on 27 July 2021).
55. Equilibrium Line | Vatnajökull National Park. Available online: <https://www.vatnajokulsthjodgardur.is/en/areas/melting-glaciers/glaciology/equilibrium-line> (accessed on 2 August 2021).
56. Gudmundsson, S.; Sigmundsson, F.; Carstensen, J.M. Three-dimensional surface motion maps estimated from combined interferometric synthetic aperture radar and GPS data. *J. Geophys. Res. Solid Earth* **2002**, *107*, ETG 13-1–ETG 13-14. [[CrossRef](#)]
57. Gernhardt, S.M. High Precision 3D Localization and Motion Analysis of Persistent Scatterers Using Meter-Resolution Radar Satellite Data. Ph.D. Thesis, Technical University of Munich, Munich, Germany, 2011.